Data-based estimates of interannual sea–air CO_2 flux variations 1957–2020 and their relation to environmental drivers

Christian Rödenbeck[1], Tim DeVries[2], Judith Hauck[3], Corinne Le Quéré[4], and Ralph F. Keeling[5]

[1]Max Planck Institute for Biogeochemistry, Jena, Germany
[2]Department of Geography, University of California, Santa Barbara, USA
[3]Alfred Wegener Institute Helmholtz Centre for Polar and Marine Research, Bremerhaven, Germany
[4]School of Environmental Sciences, University of East Anglia, Norwich, UK
[5]Scripps Institution of Oceanography, University of California, San Diego, USA

Correspondence to: C. Rödenbeck (christian.roedenbeck@bgc-jena.mpg.de)

Abstract. This study considers year-to-year and decadal variations as well as secular trends of the sea–air CO_2 flux over the 1957–2020 period, as constrained by the pCO_2 measurements from the SOCATv2021 data base. In a first step, we relate interannual anomalies in ocean-internal carbon sources and sinks to local interannual anomalies in sea surface temperature (SST), the temporal changes of SST (dSST/dt), and squared wind speed (u^2), employing a multi-linear regression. In the tropical Pacific, we find interannual variability to be dominated by dSST/dt, as arising from variations in the upwelling of colder and more carbon-rich waters into the mixed layer. In the eastern upwelling zones as well as in circumpolar bands in the high latitudes of both hemispheres, we find sensitivity to wind speed, compatible with the entrainment of carbon-rich water during wind-driven deepening of the mixed layer and wind-driven upwelling. In the Southern Ocean, the secular increase in wind speed leads to a secular increase in the carbon source into the mixed layer, with an estimated reduction of the sink trend in the range 17 to 42%. In a second step, we combined the result of the multi-linear regression and an explicitly interannual pCO_2-based additive correction into a "hybrid" estimate of the sea–air CO_2 flux over the period 1957–2020. As a pCO_2 mapping method, it combines (a) the ability of a regression to bridge data gaps and extrapolate into the early decades almost void of pCO_2 data based on process-related observables and (b) the ability of an autoregressive interpolation to follow signals even if not represented in the chosen set of explanatory variables. The "hybrid" estimate can be applied as ocean flux prior for atmospheric CO_2 inversions covering the whole period of atmospheric CO_2 data since 1957.

1 Introduction

The atmospheric CO_2 content has risen during the recent decades, primarily due to anthropogenic emissions (IPCC, 2013). However, the actual rise has been co-determined by the exchange of CO_2 between the atmosphere and natural systems, notably the ocean and the land vegetation. The uptake of atmospheric CO_2 into the ocean is primarily driven by the solution disequilibrium across the sea–air interface. As the surface-ocean carbon content is lagging behind the atmospheric rise, the ocean uptake is, to first order, increasing in parallel with the atmospheric CO_2 rise. However, natural climate variability and anthopogenic climate change alter the uptake rate on year-to-year and decade-to-decade time scales as well as in its secular

evolution. This leads to a feedback loop: Atmospheric CO_2 influences the climate via the greenhouse effect, while the climate in turn influences the carbon-relevant natural systems in the ocean and on land. This feedback loop could dampen or accelerate climate change.

In order to understand the future climate trajectory, therefore, we need to quantitatively understand the carbon response of the natural systems. For example, how will secular trends towards higher wind speeds in the Southern Ocean affect the sea–air CO_2 exchange in this region (Le Quéré et al., 2007; Hauck et al., 2013, and many others)? While the relevant time scale is secular (multi-decadal) trends, year-to-year or decade-to-decade variability in CO_2 fluxes can be used as "natural experiments" to understand the climatic controls of the land and ocean carbon cycle. This can be done by quantifying variations of carbon fluxes from suitable observations, and statistically relating them to variations in quantities describing relevant environmental conditions. Even though the climate–carbon cycle feedback loop involves the global CO_2 fluxes only (because atmospheric CO_2 is mixed globally within about one year), the statistical analysis needs to be done on a spatial scale fine enough to accomodate the spatial inhomogeneity of the involved processes.

Suitable observational data therefore need to provide sufficient spatial and temporal detail and span several decades. Regarding ocean CO_2 fluxes, there are essentially two types of such data: (1) Sustained *atmospheric* CO_2 *measurements* at various locations worldwide (Keeling, 1978; Conway et al., 1994; Francey et al., 2003, and many more) and (2) sustained and spatially extensive measurements of the CO_2 *partial pressure (pCO$_2$) in the surface ocean* (Bakker et al., 2016). As changes and gradients in atmospheric CO_2 reflect the sum of the regional CO_2 sources and sinks at the surface, atmospheric CO_2 data have been combined with simulations of atmospheric tracer transport and inverse techniques to estimate spatial and temporal variations of the CO_2 fluxes ("atmospheric inversion", Newsam and Enting, 1988; Rayner et al., 1999; Bousquet et al., 2000; Rödenbeck et al., 2003; Baker et al., 2006, and many others). Even though most of the atmospheric inversions start in the 1990s or 2000s when more and more stations became operational, the longest time series of atmospheric CO_2 measurements are available since 1957 (as used in Rödenbeck et al., 2018a). However, atmospheric inversions are known to have limited capability to correctly assign signals to land or ocean (Peylin et al., 2013). While the resulting error is relatively small for the land fluxes, it strongly affects the estimated ocean flux variability, because the ocean variability is much smaller than the land variability.

Therefore, the surface-ocean pCO_2 data (Bakker et al., 2016) currently provide the most detailed information about the spatio-temporal variability of the sea–air CO_2 exchange. To cope with the very inhomogeneous distribution of these pCO_2 data in space and time, including substantial gaps, several methods have been developed to map (interpolate) the data into continuous spatio-temporal fields of pCO_2 (Takahashi et al., 2009; Watson et al., 2009; Valsala and Maksyutov, 2010; Landschützer et al., 2013; Nakaoka et al., 2013; Rödenbeck et al., 2013; Majkut et al., 2014; Iida et al., 2015; Jones et al., 2015; Zeng et al., 2015; Denvil-Sommer et al., 2019; Gregor et al., 2019, and several others). Most of these mappings employ either (i) an auto-regressive interpolation that fills unobserved areas or periods based on the neighbouring data within some prescribed correlation radii in space and time, or (ii) a regression of pCO_2 against suitable explanatory variables that have been observed more densely and over all the target period (using linear regression, neural networks, or machine learning). These two types of mappings offer complementary advantages, as regressions against explanatory variables possess predictive skill allowing

to fill longer data gaps (and potentially to extrapolate into data-void periods), while auto-regressive mappings can reproduce all signals in the data even if not represented in the chosen explanatory variables (Rödenbeck et al., 2015). From the mapped pCO_2 fields, the sea–air CO_2 flux is then calculated via a gas-exchange parameterization. In addition to studying the ocean carbon cycle, these flux estimates have also been used as an interannually varying ocean prior in atmospheric CO_2 inversions

5   to potentially improve land CO_2 flux estimates (Rödenbeck et al., 2014).

With regard to the aim of understanding how the oceanic carbon cycle may respond to decadal and secular climatic changes as laid out above, however, the current pCO_2 mappings have two limitations. As a first limitation, the current pCO_2 mappings only provide spatio-temporal variations in the pCO_2 field and the sea-air CO_2 flux, but do not explicitly quantify the relationships between these variations and underlying environmental drivers. This is true even for the regressions against

10   explanatory variables: Even though these relationships are implicitly contained in the synaptic weights of neural networks or similar parameters in machine learning algorithms, they are not accessible from these algorithms in interpretable form.

The second limitation arises from the fact that very little pCO_2 data exist before the mid 1980s (Bakker et al., 2016). In the equatorial Pacific, critical due to its large variability, sufficient coverage does not start before 1992. Despite their predictive skill, even the available pCO_2 regressions against explanatory variables only cover a time period not longer or even shorter

15   than the pCO_2 data period, some for example because chlorophyll-a data have only been available in the satellite era since 1997. Thus, none of the currently available pCO_2 mappings starts before 1980. Consequently, they cannot be used as a data-based ocean prior in atmospheric CO_2 inversions over the full period of atmospheric data (1957–present). Further, the pCO_2 mappings do not cover the 1960–present period considered in ongoing synthesis projects like the annual carbon budget by the Global Carbon Project (GCP) (Friedlingstein et al., 2020), which so far exclusively relies on process model simulations during

20   the first decades.

As a contribution to overcome these two limitations, this study has a two-fold aim:

– First, extending the CarboScope pCO_2 mapping (Rödenbeck et al., 2013, 2014), we have developed a multi-linear regression explicitly estimating the sensitivities of the carbon sources and sinks in the oceanic mixed layer against the variations in relevant explanatory variables. This allows a data-based view on the processes plausibly underlying year-

25   to-year variability in different parts of the ocean.

– Second, we have combined this multi-linear regression with an additive auto-regressive correction into a "hybrid" mapping, inheriting the complementary advantages of both auto-regressive and regression-based pCO_2 mappings. As the regression extrapolates the variability back to 1957 by only using explanatory variables available throughout all this time frame, the hybrid mapping yields an observation-based estimate of the spatio-temporal variability of sea–air CO_2

30   fluxes since 1957.

After describing the mapping methods (Sect. 2), we present how the multi-linear regression traces the origin of interannual variations in the oceanic carbon system to the individual environmental quantities used as explanatory variables (Sect. 3.1). We present the spatial patterns in the regression coefficients (sensitivities) and discuss possible underlying mechanisms controlling the oceanic carbon system (Sect. 3.2). We evaluate the predictive skill of the multi-linear regression step as one of its most

important requirements (Sect. 3.3). Finally, we present the interannual variations of sea–air CO_2 fluxes estimated by the hybrid mapping (Sect. 3.4) and compare it to the variations captured by the multi-linear regression (Sect. 3.5). In the discussion, we consider whether the presented multi-linear regression indeed meaningfully reflects biogeochemical processes (Sect. 4.1), which fraction of interannual variability it is able to capture (Sect. 4.2), to which extend the sensitivities depend on time-scale (Sect. 4.3), and how some uncertainties may affect the result (Sects. 4.4–4.6). In an appendix, we focus on the global total sea–air CO_2 flux estimated by the hybrid mapping in terms of its mean (Sect. A1) and secular trend (Sect. A2), discussing its uncertainty and comparing it with literature values obtained by other methods.

2 Method

2.1 $p\mathrm{CO_2}$ mapping

2.1.1 Overview

The $p\mathrm{CO_2}$ mapping schemes used in this study are variants of the CarboScope $p\mathrm{CO_2}$ mapping described in Rödenbeck et al. (2013). The estimates are based on the $p\mathrm{CO_2}$ data (converted from the original fugacity data, see Table 1) in the SOCAT data collection version v2021 (Bakker et al., 2016, 2020). The elements common to all mapping variants are summarized in the following and illustrated in Fig. 1; for details we refer to Rödenbeck et al. (2013).

Parameterizations of sea–air gas exchange (quadratic wind speed dependence as in Wanninkhof, 1992) and solubility (Weiss, 1974), a calculation of the chemical equilibrium of the carbonate chemistry in sea water (Orr and Epitalon, 2015), as well as a mixed-layer budget of dissolved inorganic carbon (DIC) (Rödenbeck et al., 2013), are used to express the $p\mathrm{CO_2}$ field and the sea–air CO_2 flux field as a function of the ocean-internal flux of DIC, f_{int} (Fig. 1). The ocean-internal DIC flux f_{int} is meant to comprise all sources and sinks of DIC into or out of the oceanic mixed layer, through biological conversion within the mixed layer or through mixing-in of waters with different DIC concentration. It is expressed as the sum of a fixed (a-priori) flux field and a set of predefined spatio-temporal patterns of adjustment each scaled by an adjustable parameter (the sets of patterns are detailed for each variant of the mapping below). Then, the mismatch between the calculated $p\mathrm{CO_2}$ field (at the respective pixels and time steps containing the SOCAT $p\mathrm{CO_2}$ samplings) and the corresponding measured $p\mathrm{CO_2}$ values (black dots in the $p\mathrm{CO_2}$ panel of Fig. 1) is gauged by a quadratic cost function. The (a-posteriori) estimates of the mapping are calculated from those values of the adjustable parameters that minimize this cost function. In the example of Fig. 1, the two estimates (colored) follow the data points (black dots) more closely than the prior (grey).

Spatial and temporal interpolation between the very inhomogeneously sampled data is implemented in the following way. By choosing a set of spatial patterns of adjustment that are centered at all the individual ocean pixels but simultaneously affect the respective neighbouring pixels within some correlation radius (to be detailed below), in conjunction with additional Bayesian terms in the cost function that penalize large adjustments to the adjustable parameters, the parameter fields (the ocean-internal DIC flux field or the fields of sensitivities, respectively, see below) are forced to be smooth. These smoothness constraints spread the information from data-covered pixels to neighbouring unconstrained pixels (see Fig. 5 of Rödenbeck

et al., 2013), thereby interpolating spatial data gaps. (The set of patterns of adjustment indirectly defines the Bayesian a-priori covariance matrix, see Rödenbeck, 2005, for background.) Interpolation in time is achieved analoguously by temporal smoothness constraints (even though, for practical reasons, a mathematically equivalent Fourier formulation is used).

The four mapping variants used here differ in the choices of the prior for f_{int} and the set of spatio-temporal patterns of adjustment. Our development started from a variant (Sect. 2.1.2) essentially identical to Rödenbeck et al. (2013) used as the CarboScope pCO_2 mapping before version v2020, except for some technical changes described later (Sect. 2.1.6–2.1.7). As an intermediate modification, we introduced a prior stabilizing the secular trend (Sect. 2.1.3); the result of this variant will be used to help discussing specific aspects. The main results of this study come from the multi-linear regression (Sect. 2.1.4) and the hybrid mapping (Sect. 2.1.5). Fig. 2 summarizes the differences and the flow of information between the four variants.

2.1.2 The "Zero-prior Explicitly interannual" pCO_2 mapping (ZE)

The starting variant has a general set of (many) patterns of adjustment, allowing an arbitrary smooth spatio-temporal internal DIC flux field f_{int}^{ZE} (Rödenbeck et al., 2013). This field f_{int}^{ZE} is implemented as the sum of a constant term (subscript 'LT' for 'long-term') and terms for seasonal (subscript 'Seas') and interannual anomalies (non-seasonal, subscript 'IAV'),

$$
\begin{aligned}
f_{int}^{ZE}(x,y,t) &= f_{int,IAV}^{adj}(x,y,t) \\
&+ f_{int,LT}^{ADJ}(x,y) + f_{int,Seas}^{ADJ}(x,y,s)
\end{aligned}
\tag{1}
$$

As indicated by the superscript 'adj' or 'ADJ' (difference explained below), all these terms involve degrees of freedom being adjusted in the cost function minimization sketched above. A-priori, all adjustable terms are zero, such that the prior of f_{int}^{ZE} is zero as well.

The interannual term $f_{int,IAV}^{adj}(x,y,t)$ can represent non-seasonal anomalies on all month-to-month, year-to-year, or decadal time scales, including secular trends. The level of its temporal smoothness corresponds to a-priori correlation length scales of about 4 weeks, implemented through a mathematically equivalent Fourier series with dampened higher-frequency components (where Fourier terms dampened to less than 2% are discarded entirely). This amounts to 722 scalable Fourier terms for our 71-year calculation period 1951–2021. The seasonal term $f_{int,Seas}^{ADJ}$ only contains seasonal Fourier components; thus it only depends on the time s within the year and repeats itself every year. Along the seasonal cycle, it has the same temporal correlation length as the interannual term of about 4 weeks, amounting to 10 scalable Fourier terms. The constant term $f_{int,LT}^{ADJ}$ is not time-dependent by definition (1 temporal degree of freedom).

Spatially, the level of smoothness in all three terms corresponds to a-priori correlation length scales of about $640\,km$ in longitude and latitude.

As symbolized by the capitalized superscript 'ADJ', the a-priori uncertainties of the seasonal Fourier terms of $f_{int,LT}^{ADJ}$ and $f_{int,Seas}^{ADJ}$ are chosen to be enlarged relative to the non-seasonal Fourier terms of $f_{int,IAV}^{adj}$, corresponding to larger expected amplitudes of seasonal variations in f_{int} compared to non-seasonal ones. In terms of the implied a-priori autocorrelation function, these enhanced a-priori uncertainties of seasonal variations are equivalent to non-zero temporal correlations between the flux at any given time-of-year and the same time-of-year in all other years (in addition to the 4-weeks decaying correlations

mentioned above). Due to these periodic correlations, f_{int} in time periods without data does not fall back to the prior (here zero) but to the mean seasonal cycle $f_{\text{int,Seas}}^{\text{ADJ}}$ as constrained by the data-covered periods.

2.1.3 The "Explicitly interannual" $p\text{CO}_2$ mapping (E)

In order to stabilize the secular trend in the early decades (as discussed in Sect. A2 below), we now add a fixed (ie., non-
5 adjustable) term (superscript 'fix'),

$$
\begin{aligned}
f_{\text{int}}^{\text{E}}(x,y,t) \;=\;& f_{\text{int,IAV}}^{\text{adj}}(x,y,t) \\
+\;& f_{\text{int,LT}}^{\text{ADJ}}(x,y) + f_{\text{int,Seas}}^{\text{ADJ}}(x,y,s) \\
+\;& f_{\text{int,Decad}}^{\text{fix=OCIM}}(x,y,t)
\end{aligned}
\tag{2}
$$

Consequently, the prior of $f_{\text{int}}^{\text{E}}$ is given by this fixed term. It is obtained from the sea–air flux product by DeVries (2022), which
10 is based on an abiotic carbon cycle model that captures the rising atmospheric CO_2 boundary condition and is embedded in a data-driven model of time-mean ocean circulation (OCIM). The OCIM fluxes have been decadally smoothed (indicated by subscript 'Decad'), because the OCIM result originally represents sea–air fluxes including SST-related interannual variations, which are created by our parameterizations already (Fig. 1).

2.1.4 The "multi-linear Regression" (R)

15 In the third variant, the ocean-internal DIC flux is represented as

$$
\begin{aligned}
f_{\text{int}}^{\text{R}}(x,y,t) \;=\;& \sum_i \gamma_i^{\text{adj}}(x,y) \cdot V_i(x,y,t) \\
+\;& f_{\text{int,LT}}^{\text{ADJ}}(x,y) + f_{\text{int,Seas}}^{\text{ADJ}}(x,y,s) \\
+\;& f_{\text{int,Decad}}^{\text{fix=OCIM}}(x,y,t)
\end{aligned}
\tag{3}
$$

Compared to Eq. (2), the degrees of freedom representing interannual variations ($f_{\text{int,IAV}}$) are replaced here by a multi-linear
20 function involving three explanatory fields (V_i):

- Sea surface temperature (SST),

- its temporal change (dSST/dt), and

- squared wind speed (u^2).

There is a two-fold motivation behind this choice of explanatory variables: (1) Variations in carbon-relevant processes (e.g.,
25 carbon and nutrient input into the mixed layer, stratification, mixing, entrainment, wind-driven deepening of the mixed layer) are expected to also be related to these variables. (2) Observation-based data sets for SST and u are available over all our calculation period 1951–2021 (u at least from reanalysis). The specific input data sets used in our base case are given in Table 1.

The simultaneous use of SST and dSST/dt is motivated as it is *changes* in SST that are related to DIC fluxes (i.e., *changes* in DIC). Moreover, the sum of SST and dSST/dt mathematically allows a temporal shift between SST and f_{int} for a dominant Fourier mode (similar to sine and cosine terms).

To prevent confusion, we point out that the multi-linear regression as introduced here is set up in terms of the ocean-internal DIC flux f_{int} (see Sect. 2.1.1), not in terms of pCO_2 or sea–air flux as done in various other studies in the literature. This also means that important processes (SST-dependence of solubility and carbonate chemistry, wind speed dependence of gas exchange) are not included into the regression Eq. (3), but already taken care of by the parameterizations listed in Sect. 2.1.1 and Fig. 1.

All the explanatory fields V_i are implemented on monthly time scale, smoothly transformed onto our daily time steps. The scaling factors γ_i^{adj} between the internal DIC flux and these explanatory fields V_i are taken as the adjustable degrees of freedom in the cost function minimization (very analoguous to the "NEE-T inversion" of Rödenbeck et al., 2018b). These unknown scaling factors are allowed to vary spatially (with correlation length of about $2000\,km$ in longitude and $1000\,km$ in latitude, thus more smoothly than the direct adjustments of f_{int} in the explicitly interannual mapping of Sect. 2.1.3), but are constant in time (1 temporal degree of freedom per explanatory field per pixel). All three regression terms are normalized such that the a-priori uncertainty of their global integral on July 1 (averaged over the July 1 time steps of all years within the analysis period 1957–2020) is the same as that of $f_{int,IAV}$ in Eq. (2). (July 1 is an arbitrary choice, in line with the normalization with respect to the flux at mid of the final year used in CarboScope so far).

In order to avoid influences of the spin-up transient on the regression coefficients (estimated sensitivities), the regression terms (first line of Eq. (3)) are only covering the analysis period 1957–2020, while the remaining years before and after are filled by explicitly interannual degrees of freedom just as $f_{int,IAV}^{adj}$ in Eq. (2). For clarity, this detail has been omitted from Eq. (3).

2.1.5 The "Hybrid" pCO_2 mapping (H)

The final variant aims to combine the temporal extrapolation capability of the multi-linear regression (Sect. 2.1.4) and the flexibility to reproduce observed signals of the explicitly interannual mapping (Sect. 2.1.3). Technically being an explicitly interannual mapping itself, its representation of the ocean-internal DIC flux,

$$
\begin{aligned}
f_{int}^H(x,y,t) \;=\; & f_{int,IAV}^{adj}(x,y,t) \\
+\; & f_{int,LT}^{adj}(x,y) + f_{int,Seas}^{adj}(x,y,s) \\
+\; & f_{int}^{fix=R}(x,y,t)
\end{aligned}
\tag{4}
$$

is similar to Eq. (2), but with the following two changes:

– As the essential change, the interannually varying result of the multi-linear regression (Sect. 2.1.4) is used as prior for the internal DIC flux ($f_{int}^{fix=R}(x,y,t)$), instead of the decadally smoothed OCIM result only containing decadal variations and the secular trend.

– As a merely technical change, the a-priori uncertainties of the mean flux $f_{\mathrm{int,LT}}^{\mathrm{adj}}(x,y)$ and the seasonality $f_{\mathrm{int,Seas}}^{\mathrm{adj}}(x,y,s)$ are not enhanced with respect to non-seasonal variability $f_{\mathrm{int,IAV}}^{\mathrm{adj}}(x,y,t)$ any more (indicated by the lower-case superscript 'adj' in all three terms), because the prior $f_{\mathrm{int}}^{\mathrm{fix=R}}(x,y,t)$ already contains a long-term mean and a mean seasonal cycle.

In essence, the hybrid mapping thus adds an interannually varying correction to the multi-linear regression. Due to this construction, the hybrid result will fall back to the multi-linear regression during periods without data, but it is nevertheless able to fit pCO_2 signals on month-to-month, year-to-year, and decadal time scales that have not yet been reproduced via the explanatory variables of the multi-linear regression.

Methodological note: Mathematically, the hybrid run is equivalent to estimating the additive correction to the multi-linear regression from the pCO_2 residuals of the multi-linear regression. That is, the signals being used by the hybrid run are those that could not yet be explained by the multi-linear regression. The hybrid run is thus similar to a hypothetical joint run simultaneously having regression degrees of freedom (like the multi-linear regression) and explicitly interannual degrees of freedom (like the explicitly interannual estimate). We abandoned the concept of such a joint run, however, because it would face two problems: (1) its result would depend on the relative a-priori weighting between the two groups of degrees of freedom, for which there is no clear information; and (2) the explicitly interannual degrees of freedom would necessarily also absorb part of the signals actually proportional to the explanatory variables. Running the multi-linear regression and the hybrid step sequentially, as done here, reduces both problems.

2.1.6 The Pre-mapping (P): Determining the linearization of the carbonate chemistry

In contrast to Rödenbeck et al. (2013), we now allow for the secular trend in the Revelle factor. We deem this necessary due to our longer period of interest 1957–2020, during which the mixed-layer carbon content notably increased, leading to shifts in the relation between variations in the ocean-internal DIC flux (f_{int}) and the sea–air CO_2 flux. As our scheme extrapolates the seasonality (and in the "multi-linear regression" also the interannual variations) from the data-constrained recent decades to the almost unconstrained earlier decades through correlations in f_{int} (see the last paragraph of Sect. 2.1.2), the shifting relation has the potential to alter the amplitude of flux variations in the earlier decades.

As in Rödenbeck et al. (2013), the non-linear dependence of pCO_2 on DIC is linearized around reference fields $pCO_{2\mathrm{Ref}}$ and DIC_{Ref},

$$pCO_2 = pCO_{2\mathrm{Ref}} + \left(\frac{\mathrm{d}pCO_2}{\mathrm{dDIC}}\right)(DIC - DIC_{\mathrm{Ref}}) \tag{5}$$

The linearization is needed to be able to use the fast minimization algorithm in the CarboScope software. Previously in Rödenbeck et al. (2013), the reference fields $pCO_{2\mathrm{Ref}}$ and DIC_{Ref} were temporally constant, had been taken from observation-based data sets not guaranteed to be mutually consistent, and the derivative ($\mathrm{d}pCO_2/\mathrm{dDIC}$) had been calculated from these via approximation formulas. In order to now include the secular trend in Revelle factor (and simultaneously to remove the mentioned approximations), we employ the *mocsy* package (Orr and Epitalon, 2015), which provides routines to accurately calculate pCO_2 and ($\mathrm{d}pCO_2/\mathrm{dDIC}$) from a given field of DIC (and from fields of Alkalinity, SST, salinity, silicate, phosphate, and air pressure, which we take from external sources, Table 1). Using an adjusted Newton algorithm calling *mocsy* iteratively,

we obtain an algorithm to calculate (reference) DIC and $(\mathrm{d}p\mathrm{CO}_2/\mathrm{dDIC})$ from a given (reference) $p\mathrm{CO}_2$ value at each location and time (box L in Fig. 2). The $p\mathrm{CO}_{2\mathrm{Ref}}$ field is obtained as the posterior $p\mathrm{CO}_2$ field of a "pre-mapping" run (P, the leftmost one in Fig. 2). The $p\mathrm{CO}_{2\mathrm{Ref}}$ and $(\mathrm{d}p\mathrm{CO}_2/\mathrm{dDIC})$ fields used in this pre-mapping run, in turn, are calculated from a preliminary reference identical to atmospheric $p\mathrm{CO}_2$. This yields a reasonable starting point, because the atmospheric $p\mathrm{CO}_2$ field does 5 already contain the secular CO_2 rise, which is the most important feature in this context.

Potentially, we might expect to need a loop with further pre-mappings, each getting its $p\mathrm{CO}_{2\mathrm{Ref}}$ field from the posterior $p\mathrm{CO}_2$ field of the respective previous one. However, we confirmed by explicit testing that the fields are not appreciably altered any more after the first pre-mapping; thus a single pre-mapping is sufficient.

All other mapping runs of this study use the same spatio-temporal linearization fields $p\mathrm{CO}_{2\mathrm{Ref}}$, $\mathrm{DIC}_{\mathrm{Ref}}$, and $(\mathrm{d}p\mathrm{CO}_2/\mathrm{dDIC})$ 10 as calculated by the pre-mapping.

2.1.7 Technical details common to all variants

As in Rödenbeck et al. (2013), the $p\mathrm{CO}_2$ data comprise the individual observations from file "https://www.ncei.noaa.gov/data/oceans/ncei/ocads/data/0235360/SOCATv2021.tsv", including all observations flagged A-D. The additional file flagged E was not used.

15 In contrast to Rödenbeck et al. (2013), the analysis period now starts in 1957 (chosen in light of the potential use of the results as prior in atmospheric inversions). The actual calculation period of all runs starts in 1951. According to explicit tests, this allows the initial transient of the mixed-layer DIC budget equation to decay by 1957. As in Rödenbeck et al. (2013), the calculation period includes one more year ("spin-down", here 2021) after the valid period constrained by the data (until end of 2020), in order to avoid numerical edge effects.

20 In order to cover all the calculation period since 1951, we now use SST from Hadley EN.4.2.1 (Good et al., 2013) and sea ice concentration from HadISST 2.2.0.0. (Titchner and Rayner, 2014, accessed on 2020-06-05 from https://www.metoffice.gov.uk/hadobs/hadisst2/data/HadISST.2.2.0.0_sea_ice_concentration.nc.gz).

Compared to Rödenbeck et al. (2013), the spatial resolution of all the mapping calculations has been increased to $2.5°$ longitude $\times 2°$ latitude (previously on the grid of the TM3 atmospheric transport model, $5° \times 4°$). Moreover, the adjustments 25 are now done over the entire ocean (i.e., we do not fix part of the temporally ice-covered regions any more).

2.2 Uncertainty and test cases

In order to explore how robust the results of the multi-linear regression (Sect. 2.1.4) are, we also perform *uncertainty cases* where certain set-up parameters are modified within ranges deemed as plausible as the base case:

RegrSSTNOAA: using SST from NOAA_ERSST v5 Huang et al. (2017) as alternative data set for the explanatory variables 30 SST and dSST/dt (but no change to any other SST-dependent items such as solubility);

RegrU2NCEP: using wind speeds from NCEP reanalysis (Kalnay et al., 1996) as alternative data set for the explanatory variable u^2 (but no change to wind-dependent gas exchange);

RegrAdddSSTdt2: Additional regression term based on $(\mathrm{d}SST/\mathrm{d}t)^2$;

RegrAddU4: Additional regression term based on u^4;

RegrAddpaCO2: Additional regression term based on decadally smoothed $p_a\mathrm{CO}_2$;

RegrNoDecad: removing any decadal variability and secular trends from the explanatory fields V_i, such that the multi-linear regression term only represents interannual variability on a time scale of a few years;

RegrShort: shorter spatial correlation lengths for the sensitivities γ_i^{adj} (supplementary Fig. S5);

RegrLoose: a-priori uncertainty of the sensitivities increased by a factor 4 (i.e., the strength of the mathematical regularization is reduced);

MLDq2: Dividing mixed-layer depth by 2;

MLDx2: Multiplying mixed-layer depth by 2 (lacking a clear uncertainty range of mixed-layer depth, MLDq2 and MLDx2 represent a rather strong change, maybe already outside the actual uncertainty);

GasexLow: Weaker gas exchange, by scaling the gas transfer velocity field such that its global mean matches the lower limit of the range $16.5 \pm 3.2\,\mathrm{cm/hr}$ (Naegler, 2009) rather than the central value;

GasexHigh: Stronger gas exchange (analoguously, using upper limit);

GasexU1: Replacing the u^2 dependence of gas exchange by a $|u|$ dependence (while keeping the global mean gas transfer velocity the same).

GasexU3: Replacing the u^2 dependence of gas exchange by a $|u|^3$ dependence (while keeping the global mean gas transfer velocity the same).

To help in the discussion of specific aspects, we performed further *test cases* (not necessarily as plausible as the base case):

RegrOnlySST, RegrOnlydSSTdt, RegrOnlyU2: The explanatory variables were used individually, i.e., the regression terms of the remaining two were omitted;

RegrAddChl_98r19: Addition of Chl-a as a further explanatory variable (Fig. S7). Chlorophyll concentration has been taken from the GlobColour project (Maritorena et al., 2010), which combined retrievals from the SeaWiFS (NASA), MODIS (NASA), MERIS (ESA), OLCI (ESA), and VIIRS (NOAA/NASA) satellites into a harmonized data set; as the Chl-a data are only available for the years 1998–2019, the regression is restricted to this period (plus spin-up and spin-down periods);

RegrHeat_85r09: replacing dSST/dt with the net sea–air heat flux taken from the OAFlux project (Yu and Weller, 2007), regression period restricted to 1985–2009 according to the availability of the heat flux data set;

RegrCurl_88r18: replacing u^2 with windstress curl calculated from Cross-Calibrated Multi-Platform (CCMP) v2.0 wind speeds (Atlas et al., 2011), regression period restricted to 1988–2018 according to the availability of CCMP;

98r19, 85r09, 88r18: Using the same regression terms as in the base case, but restricting the time period of regression to the same years as used for RegrAddChl_98r19, RegrHeat_85r09, and RegrCurl_88r18, respectively.

5   Uncertainties in the hybrid mapping (Sect. 2.1.5) were explored analoguously by re-running the hybrid step with several of the uncertainty cases of the regression listed above. Part of the involved set-up changes (mixed-layer depth, gas exchange) also affect the hybrid calculation itself.

2.3   Gauging the predictive skill of the multi-linear regression

In order to test whether the multi-linear regression against explanatory variables (Sect. 2.1.4) is actually meaningful, we
10   determine its predictive skill. For this, the multi-linear regression is re-run 6 times, each time omitting the pCO_2 data from one of the 5-year periods 1985–1989, 1990–1994, 1995–1999, 2000–2004, 2005–2009, or 2010–2014. That is, each of the 6 test runs possesses an artificial data gap of 5 years, a duration chosen to be longer than typical features of year-to-year variability like El Niño. We can then compare the predictions during the data gaps with the results of the completely constrained run.

3   Results

15   The main results of this study are of two different types:

  – From the *multi-linear regression*, we obtain spatial maps of the sensitivities γ_i (Eq. (3)) relating the variations in the surface-ocean carbon system to variations in SST, dSST/dt, and u^2 (Sect. 3.2).

  – The *hybrid mapping* yields a spatio-temporal estimate of the sea–air CO_2 flux over 1957–2020, in particular its evolution from year to year (Sect. 3.5).

20   Further results are presented for illustration and to elucidate the robustness of the main results.

3.1   Origin of interannual variations as estimated by the multi-linear regression

The multi-linear regression attempts to trace the interannual variations in the surface-ocean carbon system (and hence in the sea–air CO_2 flux) to the interannual variations in the chosen explanatory variables SST, dSST/dt, and u^2. In Fig. 3 (left panels), the estimated contributions of the three explanatory variables to the ocean-internal DIC flux are depicted for a subdivision of the
25   ocean into 5 latitudinal bands. In the center panels, the resulting contributions to the sea–air CO_2 flux are shown, as calculated by the parameterizations and the budget equation in our mapping scheme (Sect. 2.1.1). These contributions and the prior sum up to the total sea–air CO_2 flux, shown on the right panels together with our set of uncertainty results (Sect. 2.2).

When disregarding the secular increase in the ocean carbon sink, the largest year-to-year variations of the regionally integrated sea–air carbon flux are found in the tropics (Fig. 3, middle right), in particular the tropical Pacific. Correspondingly,

the year-to-year variations in the ocean-internal carbon flux (f_{int}) from the three terms in the multi-linear regression (Eq. (3)) are largest in the tropics as well (Fig. 3, middle left). Of the three explanatory variables, the contribution of year-to-year variability in temporal SST changes (dSST/dt, black) is the largest. Concurrent with the warming (dSST/dt>0) at the onset of each El Niño event (grey background stripes), we find a negative carbon flux anomaly (reduction of the carbon source in this region) because

5   smaller amounts of cold, carbon-rich water are upwelling. At the end of each El Niño event, we find an analoguous coupling of the cooling (dSST/dt<0) and an additional carbon source to the mixed layer. The contribution of year-to-year variability in SST itself (red) is second largest in the tropics, causing anomalous carbon sinks during El Niño events and anomalous carbon sources during La Niña conditions afterwards. This could be interpreted as a small correction to the dSST/dt contribution: the sum of the dSST/dt and SST contributions (not shown) is similar to the dSST/dt contribution alone, but slightly shifted in time

10   by a few months. The smallest contribution to the year-to-year variability in the tropics is estimated for squared wind speed (u^2, light blue), with a temporal pattern relatively similar to that of the SST contribution. Due to the co-variation between SST and u^2 on year-to-year time scale, these two explanatory variables could be partly confounded by the regression, though the detailed locations where their respective sensitivities are high do not actually overlap much (see Sect. 3.2 below).

      In the high-latitude bands (top and bottom left panels of Fig. 3), the wind speed contribution is estimated to be larger than in

15   the tropics, now on the same order of magnitude as the SST and dSST/dt contributions or even larger. As a notable feature in the Southern Ocean (bottom left), the secular increase in wind speed leads to a secular increase in the carbon source into the mixed layer. Across our set of uncertainty cases (Sect. 2.2), the linear trend of the wind speed contribution over the 1960–2019 period in the ocean south of $45°\,S$ is estimated in the range 0.002 to $0.005\,(\mathrm{PgC\,yr^{-1}})\,\mathrm{yr^{-1}}$ (see supplementary Fig. S3, bottom, light blue bars). As a secular trend in f_{int} (bottom left in Fig. 3) causes a secular trend in sea–air flux of the same size (bottom

20   center), it represents a reduction by 17 to 42% of the trend towards an increasing Southern Ocean sink strength (relative to the trend of $-0.012\,(\mathrm{PgC\,yr^{-1}})\,\mathrm{yr^{-1}}$ estimated by OCIM over 1960–2019). A slowing-down of the Southern Ocean sink increase (compared to the increase expected from rising atmospheric CO_2) has also been found in model simulations and attributed to an increase in upwelling of old carbon by the accelerating winds (Le Quéré et al., 2007; Hauck et al., 2013, and many others). We need to note, however, that our multi-linear regression estimates the wind-speed related trend only indirectly: As

25   the sensitivites γ_{u^2} are presumably largely constrained by year-to-year variations (because they do not change much if the linear trend of the explanatory variables is removed, see sensitivity case RegrNoDecad, Sect. 4.3), the slope of the secular trend can only be correct to the extent that the sensitivity γ_{u^2} is identical for year-to-year and secular variations.

      The year-to-year anomalies from the f_{int} contributions (Fig. 3, left) carry through to the sea–air CO_2 flux (center) in a delayed and dampened fashion, due to the buffer effect of carbonate chemistry in combination with the limited gas exchange.

30   We also note again that the sea–air CO_2 flux contains additional year-to-year variability from solubility and gas exchange anomalies as represented by the involved parameterizations (also see Fig. 1 and Sect. 3.2.4 below).

3.2 Patterns of the sensitivity of ocean-internal DIC sources and sinks to interannual variations of SST, dSST/dt, and u^2 estimated by the multi-linear regression – which underlying processes do they suggest?

The estimated sensitivities of the ocean-internal DIC flux (f_{int}) against interannual variations in the chosen explanatory variables of the multi-linear regression (sea surface temperature SST, temporal changes in sea surface temperature dSST/dt,

5 and squared wind speed u^2) are shown in Fig. 4. Here we consider the most prominent features in these sensitivity patterns and mention oceanic processes that are compatible with these and may thus control surface-ocean biogeochemistry. Even though regression analysis cannot proof causation, we will argue later (Sect. 4.1) why such a tentative attribution may be meaningful here. Also see Sects. 4.3–4.6 for further discussion on uncertainties.

3.2.1 Sensitivity of f_{int} to dSST/dt

10 We start with dSST/dt (Fig. 4, top) as the explanatory variable contributing the largest year-to-year variability (Sect. 3.1). Events of decreasing SST are estimated to be associated with more positive ocean-internal DIC fluxes in the tropical Pacific (within a tilted band located around the equator in the western tropical Pacific and around about $15°S$ in the eastern tropical Pacific) and in most parts of the higher latitudes in both hemispheres (blue and cyan areas in Fig. 4 top). Such a correlation would arise from variations in the upwelling of waters that are both colder and more carbon-rich than the mixed layer.

15 In the rest of the ocean, the absolute value of the sensitivity $\gamma_{dSST/dt}$ is small (light blue or light red). We assume that these sensitivities mainly reflect insignificant correlations, especially due to the higher uncertainty in regions of sparse data coverage or in regions where dSST/dt is mainly driven by atmospheric heating or cooling. In particular, positive sensitivities are not compatible with any known oceanic mechanism.

3.2.2 Sensitivity of f_{int} to SST

20 The estimated sensitivity γ_{SST} between the interannual varitions of the ocean-internal DIC flux and SST itself is rather patchy, with both positive and negative areas (Fig. 4, middle). This may reflect that various biological processes contribute to f_{int}, depending on temperature in different ways and thus potentially cancelling each other. For example, carbon fixation (Net Primary Productivity, NPP) will envigorate with increasing temperature (until a threshold is reached); as NPP represents a sink (i.e., a negative contribution to f_{int}), it would thus cause negative γ_{SST} sensitivities. Carbon export (or export ratio at least) is

25 generally anticorrelated with temperature (Laws et al., 2000), thus causing positive γ_{SST} sensitivities, though also the opposite behaviour seems possible.

Positive interannual sensitivity to SST would also be compatible with a nutrient effect. Upwelling and mixing in from below both decreases SST and increases the availability of nutrients. Thus, negative anomalies in SST tend to be associated with higher biological production, thus enhanced removal of carbon (negative anomalies in f_{int}). However, upwelling also brings

30 up carbon, which is usually assumed to dominate the carbon signal. For example, Hauck et al. (2013) showed that –in the model– in the Southern Ocean south of 55° S, there would be more biological export per increase in the Southern Annular

Mode (SAM) which goes along with more upwelling. Yet, whether the carbon effect or the opposing nutrient effect dominates the upwelling signal is still controversially discussed.

As the statistical inference by our regression can only respond to the sum of all contributing processes, we therefore cannot draw specific conclusions from the estimated γ_{SST} pattern. In addition, the regression may adjust γ_{SST} to effectively shift the dSST/dt contribution in time (Sect. 3.1).

3.2.3 Sensitivity of f_{int} to u^2

Higher wind speeds are estimated to be associated with more positive ocean-internal DIC fluxes (stronger sources into or weaker sinks out of the mixed layer) along the equator in the Pacific, in the eastern upwelling zones of the North Pacific, South Pacific, and South Atlantic, as well as in circumpolar bands in the high latitudes of both hemispheres (red and yellow areas in Fig. 4 bottom). Such a positive sensitivity is compatible with wind-driven deepening of the mixed layer, Ekman pumping, or speeding up of the wind-driven upwelling, such that more carbon-rich waters are mixed in from below during stronger winds.

In contrast, higher wind speeds tend to be associated with more negative ocean-internal DIC fluxes (i.e., weaker sources or stronger sinks) at the western extratropical fringes of all ocean basins (blue areas). In these regions of mode water formation, higher wind speeds lead to more subduction of anthropogenic CO_2 away from the surface into the ocean interior.

3.2.4 Additional variability of the sea–air flux

We note again that the sensitivities discussed here are those of the ocean-internal DIC sources and sinks f_{int} (Fig. 1 bottom or Fig. 3 left). The sea–air CO_2 fluxes (Fig. 1 top or Fig. 3 center) contain additional variability also driven by interannual variations in SST (e.g., via the changes in CO_2 solubility and chemical equilibrium) or in wind speed (via the gas transfer velocity of gas exchange). As this additional variability is already generated by the parameterizations contained in our algorithm (Sect. 2.1.1), these processes are, within uncertainties, not reflected in the sensitivities against SST or u^2 again.

Even though the sea–air CO_2 flux is the quantity most directly relevant to the atmospheric CO_2 budget and its consequences for global climate, this additional variability partly disguises the variability caused by ocean-internal processes as those discussed above. This also means that the ocean-internal DIC sources and sinks f_{int} are potentially easier to be related to environmental variables than the sea–air CO_2 flux or the pCO_2 field traditionally chosen as target variable of linear or non-linear regressions because it is a directly observed quantity.

3.3 How much predictive skill does the multi-linear regression have?

The results of the multi-linear regression are only meaningful if the regression actually possesses some predictive skill to bridge unconstrained periods. Only then, they can be considered to represent generalizing relationships.

In order to test this, we performed runs with artificial data gaps of 5 years length (Sect. 2.3). Fig. 5 illustrates this using runs discarding all pCO_2 data during 1995–1999. For context, we first consider the explicitly interannual mapping (E) which draws all information about year-to-year variations from the data and therefore does not have any predictive skill. Indeed, it essentially

defaults to the prior (having upside-down El Niño response as it misses any variations related to the ocean-internal sources and sinks) during the data gap (Fig. 5 left), except for a shift in long-term mean (see Sect. 2.1.2, last paragraph, for explanation). In contrast, the multi-linear regression (Fig. 5 center) almost completely reconstructs the 1995–1999 flux variations, based on the relationships between the ocean-internal DIC flux and the driving variables learned on the basis of the remaining data outside

5   1995–1999.

As demonstrated by Fig. S1 in the supplement, this predictive skill holds generally for all parts of the ocean and other 5-year data gaps. This means that no particular pCO_2 data point is causing features in the variability and the estimated sensitivities (Sect. 3.2 above) by its own.

3.4   Sea–air CO_2 flux variations estimated by the hybrid mapping

10   After presenting the interannual sensitivities from the multi-linear regression, we now turn to interannual flux variations as estimated by the hybrid mapping involving an additional interannually varying correction (Sect. 2.1.5). Fig. 6 (blue) shows its estimated interannual (i.e., slower-than-seasonal) variations of the sea–air CO_2 flux, subdividing the ocean into basins and latitude bands. The most prominant feature of interannual variability is the secular trend towards more CO_2 uptake in all ocean regions. Considering variations around this secular trend, the tropical Pacific is the region providing the largest contribution to

15   total ocean variability (compare Le Quéré et al., 2000), both on decadal time scale and on year-to-year time scale. The year-to-year variations are strongly tied to El Niño as indicated by the background stripes (Feely et al., 1999). When considering trends within individual decades, the decadal increase in the CO_2 sink slowed down in the 1990s and early 2000s, and accelerated again afterwards (Landschützer et al., 2016; DeVries et al., 2019), even though it may be questioned whether such trends over chosen 10-year periods truely represent decadal variations rather than apparent trends arising from high-amplitude anomalies

20   on the faster year-to-year time scale.

3.5   How do the year-to-year sea–air CO_2 flux variations estimated by regression and hybrid mapping compare with each other?

In addition to the variations of the sea–air CO_2 flux estimated by the hybrid mapping (blue), Fig. 6 also shows those estimated by the multi-linear regression (Sect. 2.1.4, orange) and the explicitly interannual pCO_2 mapping (Sect. 2.1.3, green). From the

25   late 1980s onwards, when progressively more pCO_2 data are available to constrain interannual variations explicitly, the hybrid mapping (blue) shows some corrections over the multi-linear regression (orange). For the large El Niño-related variability in the tropical Pacific, these corrections are generally small compared to the estimated variations themselves. This indicates that the multi-linear regression already captures a notable fraction of the year-to-year flux variations in this region, even though it underestimates the size of most of these anomalies (the interannual standard deviation 1985–2019 from the multi-linear

30   regression is only about 82% of that from the hybrid mapping in the tropical Pacific). Fig. 7 (dots) confirms that the hybrid mapping fits the pCO_2 data closely (the blue dots are located right under the black dots), while the multi-linear regression (orange dots) also follows the variability in the data (black dots) but does not match them as closely as the hybrid mapping.

In the intermediate and high latitudes (top and bottom panels of Fig. 6), in contrast, the multi-linear regression (orange) does not pick up most of the year-to-year anomalies. This may indicate that the set of explanatory variables used in the regression misses essential modes of variability there. However, some of the variations estimated with explicitly interannual degrees of freedom (green and blue) may also be spurious effects from the temporally very uneven data coverage.

5   Although the hybrid mapping (blue) has the same interannual degrees of freedom (i.e., the same flexibility) as the explicitly interannual mapping, it does not always bring the fluxes back to the explicitly interannual result (green), especially in the region south of the tropical Pacific (Fig. 6). Since the two estimates are actually very close to each other where data exist (as illustrated in Fig. 7: the green dots are essentially invisible under the co-located blue and black dots, despite the differences between the green and blue lines), the differences in areal averages as in Fig. 6 reflect differences in data-void areas/periods being filled by

10   the mappings. However, while the explicitly interannual mapping falls back to the prior not constrained by pCO_2 data, the hybrid mapping falls back to the multi-linear regression which is at least indirectly constrained via the statistical relationships between the ocean-internal DIC flux and the chosen explanatory variables (Sect. 3.3 above). This may also prevent some undue spatial extrapolation from the tropical Pacific into unconstrained areas by the explicitly interannual scheme. Thus, we expect the hybrid mapping (blue) to be more realistic than either of the multi-linear regression and the explicitly interannual mapping

15   in terms of their detailed interannual anomalies.

In view of applying the multi-linear regression as a prior of the hybrid mapping, its predictive skill (Sect. 3.3) is only meaningful to the extent that it is actually able to explain all signals in the data. For example, since the regression underestimates the year-to-year anomalies in the tropical Pacific compared to the explicitly interannual estimate as discussed above, it will fill data gaps with somewhat too small an amplitude (Fig. 5, right). This indicates that the variability extrapolated into the earlier

20   decades without data will likely be underestimated, too, even though this is still a clear qualitative improvement compared to the explicitly interannual mapping (Fig. 5, left).

3.6   What can the pCO_2 mappings say about the secular flux trend?

In light of climate change, quantitative information about the secular flux trend are relevant. Unfortunately, as discussed in more detail in the appendix (Sect. A2), the secular trend in our mapping results is mostly determined through the prior derived

25   from the OCIM estimate based on ocean-interior data (DeVries, 2022). Due to the lack of pCO_2 data in the early decades, the mapping does not add credible information about the secular trend. Due to some slight inconsistency in the use of the prior, the secular trend is even slightly overestimated (Sect. A2); this remains to be addressed in future versions of our flux product.

4   Discussion: Robustness of the multi-linear regression

4.1   How meaningful is the multi-linear regression in terms of biogeochemical processes?

Statistical inferences by multi-linear regression are at the risk of overfitting, i.e. adjustment of coefficients to follow minor signals in the data, or even noise. If that was the case, the estimated sensitivities would not reflect underlying biogeochemical processes. Various findings indicate however that the results of the presented multi-linear regression do reflect actual signals:

- The patterns of the sensitivities (Fig. 4), at least those with respect to dSST/dt and u^2, are quite systematic spatially, and in many respects interpretable (Sect. 3.2). This is especially true in the tropical Pacific, but also throughout the entire ocean.

- Test regression runs only using a single one of the explanatory variables (RegrOnlySST, RegrOnlydSSTdt, RegrOnlyU2) yield sensitivities very similar to the base case using all explanatory variables (supplementary Fig. S2). This indicates
10 that the regression terms are essentially mutually independent, such that each explanatory variable picks up a more or less unique portion of the signals contained in the data.

- The regression possesses predictive skill (Sect. 3.3 above), which also means that it does not depend on any particular portion of the pCO$_2$ data or the explanatory fields alone.

- The estimates are relatively robust against alternative data sets for the explanatory variables (cases RegrSSTNOAA and RegrU2NCEP in supplementary Fig. S4). This corroborates that the regression is likely not dominated by any particular feature in these fields.

- The regression hardly responds to a 4-fold change in the regularization strength (case RegrLoose in supplementary Fig. S4). In the overfitting regime, one would expect a substantial dampening effect when the regularization is stronger.

- The regression results are quite robust against further changes in the set-up (supplementary Figs. S4, S5, and S6).

The relatively small set of explanatory variables used here (Sect. 2.1.4) is certainly helpful to avoid overfitting, as it means a relatively small number of degrees of freedom (compare, e.g., Thacker, 2012). Also the use of temporally constant sensitivity coefficients helps to keep the number of degrees of freedom sufficiently low. For example, in test runs with seasonally resolved sensitivity coefficients, the data could be fitted more closely, but the predictive skill deteriorated (not shown).

25   Clearly, for any given spatial area, the presence of pCO$_2$ data over a sufficient variety of environmental conditions is a prerequisite to estimate meaningful sensitivity coefficients. The "Reduction of Uncertainty" diagnostic for interannual variations given in (Rödenbeck et al., 2014) provides at least a rough indication. A "Reduction of Uncertainty" diagnostic could also be performed for the sensitivity coefficients directly, which however remains for follow-on work.

4.2 Which fraction of the year-to-year variability can be captured by the multi-linear regression?

As seen in Fig. 6 and quantified explicitly in Fig. 8 (top), the amplitude of year-to-year variability in the global sea–air CO_2 flux estimated by our multi-linear regression (orange) is lower than that estimated by the hybrid mapping possessing the degrees of freedom to follow any interannual signals (blue). This indicates that the pCO_2 data also contain signals of year-to-year variability that cannot be represented in terms of the variations contained in the set of explanatory variables used in the regression. Possibly, however, the hybrid mapping may also exaggerate the amplitude of signals by spreading them over too large an area in data-poor parts of the ocean.

The situation is different in the tropical Pacific (Fig. 8, bottom). Here, the multi-linear regression (orange) already captures a large part of the variability found in the hybrid mapping (blue). This indicates that our explanatory variables are reasonably suited to represent the ENSO-related variability dominating in this region.

To elucidate the ability of the multi-linear regression to capture year-to-year anomalies, we compare it with other pCO_2 mappings based on linear or non-linear regressions of pCO_2 (itself) against various sets of explanatory variables (Landschützer et al., 2013; Iida et al., 2020; Denvil-Sommer et al., 2019; Gregor et al., 2019). Globally (Fig. 8, top), the variability obtained by the other pCO_2 mappings (salmon) is larger than that from our multi-linear regression (orange). Closer inspection (not shown) reveals that these larger amplitudes mostly reflect variability on multi-year (decade-to-decade) time scales occurring coherently in both northern and southern extratropics, while the multi-linear regression does not involve such globally correlated contributions. Accordingly, when splitting up the global flux into regional contributions, the amplitudes from the other pCO_2 mappings and our multi-linear regression are quite comparable. For example, in the tropical Pacific (Fig. 8, bottom) our regression yields year-to-year variability larger than any of the other pCO_2 mappings considered. Based on reconstructions of model-based pseudo data, Gloege et al. (2021) found for one of the other methods included in Fig. 8 that the amplitude of Southern Ocean decadal variability was overestimated by 15 to 58%.

Could alternative or additional explanatory variables help to capture a larger fraction of variability by the multi-linear regression?

– As the explanatory variables of the base case are all physical variables, we tested using chlorophyll-a concentration as a biological variable (run RegrAddChl_98r19, supplementary Fig. S7). A practical problem with chlorophyll-a is that data sets are only available for the most recent years (from 1998); therefore it is not used in our base case. The test suggests, however, that chlorophyll is not actually adding much information about the year-to-year variations in the sea–air CO_2 flux beyond what is already provided by the explanatory variables of the base case (SST, dSST/dt, and u^2). A reason may be that chlorophyll variability is already covered in the other variables, as nutrients are also a function of upwelling and stratification etc. It is also important to keep in mind that chlorophyll concentration is not directly observed but only indirectly inferred from optical properties of the seawater. Due to that, part of the variability in the chlorophyll data may originate from processes unrelated to the carbonate system, which makes it less helpful as a predictor in the regression considered here.

– Conceivably, more general non-linear relationships between pCO_2 and the explanatory variables may allow to capture signals not represented in linear relationships as used in our base case. Uncertainty cases involving additional regression terms proportional to $(dSST/dt)^2$ (run RegrAdddSSTdt2) and $(u^2)^2$ (run RegrAddU4), respectively, only marginally increase year-to-year variability (within the narrow band in Fig. S4). Also from the set of other pCO_2 mappings (salmon in Fig. 8), there is no indication that the non-linear regressions (CMEMS-FFNN, CSIR-ML6, and MPI-SOMFFN) would generally capture more variability than the linear ones (JMA-MLR and ours). We conclude that non-linearities in the pCO_2 relationships are not essential for explaining year-to-year anomalies in the pCO_2 field on regional scale.

– Using heat flux as explanatory variable instead of dSST/dt (RegrHeat_85r09) deteriorates the ability of the multi-linear regression to reproduce ENSO-related variability (supplementary Fig. S8).

– Replacing u^2 by the windstress curl (RegrCurl_88r18) does not change the flux IAV much (supplementary Fig. S10). A further alternative explanatory variables may be "Ekman pumping", which however diverges at the equator, and was not tested.

A common methodological feature of all present-day regression-based pCO_2 mappings including ours is that the carbon variables are only related to the concurrent values of the explanatory variables, disregarding any dependence on past values of the explanatory variables possible due to memory effects. This might be a serious limitation, but allowing for memory effects is not straightforward. For example, regression terms with lagged explanatory variables would only allow discrete lag times, and using an extensive spectrum of lag times would possibly exceed the number of well-determined degrees of freedom. Theoretically, fitting comprehensive process models to the pCO_2 data would include emerging memory effects, but this faces various conceptual and computational challanges (see a recent application of a low-dimensional Green's function approach by Carroll et al., 2020). (Note that the amplitudes simulated by the hindcast ocean biogeochemical models included in Fig. 8 are roughly similar to those from our multi-linear regression and smaller than those from the hybrid scheme.) We notice that our algorithm involves some elements that do represent history effects (the budget equation (Eqn. (A18) in Rödenbeck et al., 2013) accumulating past f_{int} contributions, the seasonal "history flux" (Eqn. (A20) in Rödenbeck et al., 2013), and the use of both SST and dSST/dt as explanatory variables (see Sect. 3.1 above)). However, if memory effects are important, they are evidently not yet adequately captured by those elements.

4.3 To which extend do the sensitivities γ_i depend on time-scale?

In our formulation of the regression (Eq. (3)), the sensitivities γ_i are applied to the fields V_i of the explanatory variables including all their variations on year-to-year, decadal, and secular time scales. Conceivably, however, the relationships between f_{int} and the explanatory variables may differ for year-to-year, decadal, or secular variations. In ocean areas where the data period is long enough to possibly constrain decadal time scales directly, the estimates may therefore reflect some mixture of time scales, which would be hard to interpret.

We assessed this by the uncertainty case RegrNoDecad where any decadal variability (including any secular trend) has been removed from the 3 explanatory variables. As this case can only pick up year-to-year signals to constrain the sensitivities,

any changes compared to the base case may indicate such potential time scale conflicts. In most regions, this is not evident (supplementary Fig. S6). Exceptions are the southern Pacific and the tropical Indian (for the wind-speed sensitivity γ_{u^2}) and the western tropical Pacific (for the SST sensitivity γ_{SST}). As the explanatory variable dSST/dt, which dominates the large tropical variability, does not have much secular trend, it is not prone to time-scale dependence anyway.

5   An alternative way to assess the impact of secular trends in the explanatory variables is the uncertainty case RegrAddpaCO2 having an additional regression term proportional to decadally smoothed atmospheric CO_2 ($p_a CO_2$). As $p_a CO_2$ is rising steadily over the calculation period, this run is able to adjust the secular trend independently of the trends in SST, dSST/dt, or u^2, thus breaking any potential time scale conflicts. Indeed, the sensitivities estimated by RegrAddpaCO2 (not shown) are similar to those from the base case as well, and any differences from the base case are similar to those of RegrNoDecad.

10   We note that in ocean areas with data periods of a few years only, a possible time-scale dependence will not affect the sensitivities themselves, but it may still affect secular trends in the fluxes if sensitivities estimated for year-to-year variations are applied to secular trends in the explanatory variable. We do not have a means to detect whether this is the case.

4.4   Spurious effects from uncertainties in the parameterizations

Errors in the sea–air CO_2 flux resulting from deficiencies in our chosen parameterizations of solubility and gas exchange lead
15   to compensating spurious contributions to f_{int}, because it is the sum of both fluxes which changes the mixed-layer carbon content in our budget equation (see Fig. 1 or Rödenbeck et al., 2013). This will then also lead to spurious contributions to the estimated sensitivities γ_i. For example, spurious u^2 sensitivity may arise if the wind speed dependence of our gas exchange parameterization is not strong enough such that it is re-inforced by additional changes in the ocean-internal carbon flux (or vice versa).

20   Luckily, the interannual variability of the sea–air CO_2 flux is much smaller than that of f_{int} due to the buffer effect (see Fig. 1). Therefore, in relative terms, the error in the sea–air CO_2 flux translates into a much smaller error in f_{int} and in the sensitivities γ_i.

4.5   Spurious effects from missing interannual alkalinity variations

The estimated ocean-internal DIC flux f_{int} –and thus the estimated sensitivities γ_i in the regression– contain some spurious
25   contributions to compensate any errors in our representation of carbonate chemistry, because the $p CO_2$ data constrain the $p CO_2$ field rather than the DIC field (Fig. 1). Even though we represent the carbonate chemistry –up to the linearization– by exact equations (Sect. 2.1.6), some error arises because we only use a seasonal alkalinity climatology, while alkalinity also varies interannually due to (1) changing degrees of dilution due to freshwater fluxes (evaporation, precipitation, ice formation, and ice melt), as well as (2) mixing-in of alkalinity-rich deep waters and possibly biological influences.

30   (1) Freshwater fluxes do not only dilute alkalinity but also DIC, in equal proportions. At the same time, the sensitivities of $p CO_2$ against changes in alkalinity and DIC are almost equal in absolute value but of opposite sign (Sarmiento and Gruber, 2006). Therefore, the total effect of freshwater fluxes on $p CO_2$ is small compared to that on alkalinity and DIC, respectively.

Therefore, as we neglect both the freshwater contributions to f_{int} and the freshwater-related alkalinity variations, the combined error in pCO_2 should be small.

(2) Alkalinity variations related to mixing from below are linked to DIC variations as well, because deep waters are rich in both DIC and alkalinity, compared to the mixed layer. In contrast to the freshwater effects, however, the regression terms $\gamma_i V_i$ in Eq. (3) do contain mixing contributions to f_{int}, such that the absence of the corresponding alkalinity variations does affect our pCO_2 field being matched to the data. On the seasonal time scale (where there is no problem anyway as we are using a monthly alkalinity climatology), alkalinity variations in the tropical and subtropical oceans are dominated by freshwater effects; only at higher latitudes, alkalinity variations are increasingly affected by mixing (Lee et al., 2006). For the interannual time scales relevant here, the relative role of mixing is unclear. A better understanding –and hopefully solution– of this problem remains for further work.

We note that the spurious compensatory contributions to f_{int} do not affect the pCO_2 field being constrained by the observations. Thus, they essentially do not affect the estimated sea–air CO_2 fluxes either.

4.6 Further sources of uncertainty

The interannual variations estimated before the pCO_2 data period (i.e., before about 1990) represent extrapolations based on the estimated sensitivities γ_i and the variations in the explanatory variables. As the data sets used for the explanatory variables are generally based on fewer and more uncertain observations in the earlier decades, the uncertainty of our results is expected to be larger in the earlier decades as well. A meaningful quantification of this uncertainty is deemed impossible.

5 Conclusions

In this study, we considered the interannual variability of the sea–air CO_2 flux over the 1957–2020 period, constrained by the pCO_2 measurements from the SOCATv2021 data base (Bakker et al., 2016). Extending the pCO_2 mapping scheme of Rödenbeck et al. (2013, 2014), we employed (1) a multi-linear regression against interannual anomalies of sea surface temperature (SST), the temporal changes of SST (dSST/dt), and squared wind speed (u^2), yielding maps of interannual sensitivities, and (2) a subsequent explicitly interannual additive correction, yielding a "hybrid" estimate of spatio-temporal variations in the contemporary sea–air CO_2 flux (formal resolution 2.5° longitude × 2° latitude × 1 day).

- According to our multi-linear regression, interannual variability in the tropical Pacific is dominated by a positive correlation of ocean-internal DIC fluxes to dSST/dt, as arising from variations in the upwelling of colder and more carbon-rich waters into the mixed layer.

- In the eastern upwelling zones as well as in circumpolar bands in the high latitudes of both hemispheres, we find a positive sensitivity to wind speed, compatible with the entrainment of carbon-rich water during wind-driven deepening of the mixed layer. To the extent that this sensitivity inferred from year-to-year variations also applies to secular trends,

the wind trend in the Southern Ocean (south of 45 ° S) implies a wind-related reduction of the flux trend by about 17 to 42% (less strong increase in sink).

- As a pCO_2 mapping method, the hybrid mapping combines (a) the ability of regression to bridge data gaps and extrapolate into the early decades without much pCO_2 data constraint and (b) the ability of an autoregressive interpolation to follow signals even if not represented in the chosen set of explanatory variables. This way, at least the large contributions of the tropical Pacific to the global year-to-year variability of the oceanic CO_2 exchange can be extrapolated over all the 1957–2020 period, even though the extrapolated variability prior to about 1985 is probably underestimated.

Appendix A: The global ocean carbon sink estimated by the hybrid mapping

Here we discuss the global total of the sea–air CO_2 flux as estimated by the hybrid mapping, and compare it to various literature estimates. In order to allow a quantitative comparison, we focus on specific features, namely the mean flux (Sect. A1) and the secular flux trend (Sect. A2).

A1   The mean sink (1994–2007)

Fig. 9 shows the contemporary global sea–air CO_2 flux estimated by the hybrid mapping (blue solid bar) averaged over the 1994–2007 period. According to the set of uncertainty cases shown (blue hashed bars), the uncertainty in the mean flux from the hybrid mapping is dominated by the uncertainty of gas exchange (cases GasexLow, GasexHigh, GasexU1, and GasexU3; diagonally hashed bars), while all other uncertainty cases do not affect the mean sink estimate very much.

The spread between the flux estimates from other pCO_2 mapping methods (group of salmon bars) together with the base case of our hybrid mapping (solid blue bar) only indicates uncertainties due to the mapping algorithms, as all the estimates use the same global scaling of the gas transfer velocity from Naegler (2009). Notably, this spread does not exceed the differences due to scaling sea–air gas exchange within the uncertainty range of Naegler (2009) (cases GasexLow, GasexHigh).

The comparison between the results of the hybrid mapping and further literature values is hampered as pCO_2 mappings are estimating the total contemporary net CO_2 flux (F_{net}) through the sea–air interface, while other methods may only include certain components of it. Adopting the notation by Hauck et al. (2020), Table 3 gives the six components of F_{net} and their respective inclusion in the literature estimates considered here (note that the terms "anthropogenic" or "contemporary" are also defined differently in part of the literature).

From the increase in the anthropogenic carbon inventory in the ocean between the extensive ocean surveys in 1994 and 2007, Gruber et al. (2019) estimate an anthropogenic CO_2 uptake of $F_{ant,ss} + F_{ant,ns} = -2.6 \pm 0.3 \, \mathrm{PgC} \, \mathrm{yr}^{-1}$ over the interjacent period, shown in Fig. 9 as long-dashed line. This estimate conceptually differs from the hybrid mapping by the river-induced flux $F_{riv,ss} + F_{riv,ns}$ and the non-steady state modifications $F_{nat,ns}$ to the natural sea–air fluxes, while $F_{nat,ss}$ is zero at the global scale (Table 3). The river-induced flux is very uncertain, with literature estimates ranging between $0.45 \pm 0.18 \, \mathrm{PgC} \, \mathrm{yr}^{-1}$ (Jacobson et al., 2007) and $0.78 \pm 0.41 \, \mathrm{PgC} \, \mathrm{yr}^{-1}$ (Resplandy et al., 2018), though the real uncertainty may be even larger. If the Gruber et al. (2019) estimate is shifted by a mid-range river-induced value of $0.62 \, \mathrm{PgC} \, \mathrm{yr}^{-1}$ (resulting in the dotted

line), the base-case value from the hybrid estimate is matched more closely. Nevertheless, given the uncertainty ranges of gas exchange, river-induced outgassing, and the Gruber et al. (2019) estimate, we cannot draw any conclusions from the remaining difference.

The CO_2 flux difference between the hybrid estimate and the dotted line in Fig. 9 may also contain a contribution from systematic differences between pCO_2 in the bulk ocean water (as typically measured at a few meters depth) and pCO_2 at the diffusive surface layer (as relevant for gas exchange), arising due to systematic differences in water temperature and salinity (Woolf et al., 2016). Further, the cooler ocean skin temperature translates the atmospheric pCO_2 to a different equilibrium DIC concentration than that implicitly calculated based on bulk temperature (Robertson and Watson, 1992). Watson et al. (2020) estimated that the sum of these two effects would shift pCO_2-based estimates of the mean global CO_2 flux by -0.8 to $-0.9\,\mathrm{PgC\,yr^{-1}}$ (stronger sink). So far, however, it is unclear how well the water temperature at the relevant vertical positions can actually be determined (an important source of uncertainty not included in Watson et al. (2020)'s range) and how it varies in space and time. In any case, we note that our study mainly considers the variability of the flux, for which the effect of a time-constant correction as in Watson et al. (2020) would cancel out.

Fig. 9 further shows the global fluxes simulated by a set of Global Ocean Biogeochemical Models (GOBMs) collated in the annual Global Carbon Budget (Friedlingstein et al., 2020, mint green). Like OCIM or Gruber et al. (2019), the GOBMs results do not include the river-induced flux component, but they do conceptually include the non steady-state modification $F_{\mathrm{nat,ns}}$ of carbon uptake and natural carbon cycling (Table 3). The range of results covered by the GOBMs slightly exceeds the range of the hybrid estimates due to the gas exchange uncertainty. The median of the GOBM ensemble and the pCO_2 mapping ensemble differ by less than the mid-range river-induced value of $0.62\,\mathrm{PgC\,yr^{-1}}$.

A2 The secular sink trend (1960–2019)

Regarding the 1960–2019 secular sink trend, our estimate from the hybrid mapping (1) is not able to add much independent information, and (2) even slightly overestimates this trend relative to OCIM used in the prior:

(1) According to Fig. 10 (top), the 1960–2019 trend from the base case (blue solid bar) is quite similar to that of the base-case prior (grey open bar). Among the uncertainty cases (blue hashed bars), largest deviations are seen when mixed-layer depth is changed (MLDq2 and MLDx2); these deviations are in fact mostly inherited from their respective priors as well (not shown).

(2) Fig. 10 (top) further reveals that the prior (grey open bar) has a slightly steeper trend than the OCIM estimate (magenta), even though the prior has been derived from OCIM (Sect. 2.1.3). This discrepancy arises because we are using OCIM's sea–air fluxes as a prior of the ocean-internal flux f_{int}, even though these two quantities differ by the carbon accumulation in the mixed layer. Since the carbon accumulation accelerates (following the accelerating increase in atmospheric pCO_2), this not only leads to a difference in mean flux (Fig. 9) but also to a difference in trend. Due to the lack of information to correct the 1960–2019 secular trend from the pCO_2 data as discussed under (1), this issue leads to an overestimation of the trend in the hybrid estimate compared to OCIM. Most GOBMs (mint green) simulate an even flatter 1960–2019 trend than OCIM.

Looking at the linear trend over the better constrained more recent period 1990–2019 (Fig. 10, bottom), the estimate from the hybrid mapping becomes more independent from the prior. The pCO_2-based hybrid estimates tend to show steeper trends

than both OCIM and the GOBM simulations. Most other pCO_2 mappings (salmon) estimate the trend to be even more negative than the hybrid mapping. However, given the substantial pentade-to-pentade variations in the global flux (as reflected in the error bars), it is not fully clear how well defined the trend over the 1990–2019 period actually is.

The level of constraint in the trend over the different periods is corroborated by the "zero-prior" mapping not using the secular trend from OCIM as prior (Fig. 11). Even though the zero-prior explicitly interannual mapping (violet) and the explicitly interannual mapping (green) start from priors with very different secular trends (shown in dark and light grey, respectively), their estimated multi-decadal trends during the recent decades are still very close. In well-constrained regions like the tropical Pacific (bottom panel) they are practically identical, while some deviations occur in poorly constrained regions such as the Indian Ocean, adding up to the slight deviations in the global total flux (top). Only in the early decades where there are hardly any pCO_2 data to constrain the estimates, the two mappings stick to the differing multi-decadal trends (and also to the year-to-year variations) of their respective priors.

As the better-constrained trend over the recent decades (after about 1992) is essentially the same as that in the prior of the explicitly interannual mapping, the flat multi-decadal trend of the zero-prior mapping in the early decades is very unlikely to be true. This illustrates that a prior with the correct secular trend (such as the OCIM result used here) is indeed needed to extrapolate the ocean CO_2 sink into the data-poor first decades of our extended period of interest 1957–2020.

Data availability

The sea–air CO_2 flux estimates, mapped pCO_2 fields, as well as some auxiliary fields are available from the CarboScope website under http://www.bgc-jena.mpg.de/CarboScope/?ID=oc_v2021 where "oc_v2021" can be replaced by the other RunIDs from Table 2. Further results can be made available upon request.

Author contribution

C.R. designed and developed the pCO_2 mapping algorithm, carried out the estimation runs, and drafted the paper. All other coauthors provided important expertise to interpret the results, reviewed the draft, and gave essential support to finalize the paper.

Competing interests

The authors declare that they have no conflict of interest.

Acknowledgements. We would like to thank all contributors to the SOCAT data base, which is the basis of this work. We are grateful to J. Orr for kindly providing the code of the *mocsy* package and helping us in its use. We would like to thank R. Wanninkhof, V. Bennington, and G. McKinley for helpful community comments and discussions on our manuscript. C.L.Q. recieved funding from the Royal Society (grant

no. RP/R1/191063) and the Natural Environment Research Council Sonata project (NE/P021417/1). T.D. acknowledges support from NSF grant OCE-1948955.

The service charges for this open access publication have been covered by the Max Planck Society.

References

Atlas, R., Hoffman, R. N., Ardizzone, J., Leidner, S. M., Jusem, J. C., Smith, D. K., and Gombos, D.: A cross-calibrated, multi-platform ocean surface wind velocity product for meteorological and oceanographic applications, Bulletin of the American Meteorological Society, 92, 157–174, 2011.

Baker, D. F., Law, R. M., Gurney, K. R., Rayner, P., Peylin, P., Denning, A. S., Bousquet, P., Bruhwiler, L., Chen, Y.-H., Ciais, P., Fung, I. Y., Heimann, M., John, J., Maki, T., Maksyutov, S., Masarie, K., Prather, M., Pak, B., Taguchi, S., and Zhu, Z.: TransCom 3 inversion intercomparison: Impact of transport model errors on the interannual variability of regional CO_2 fluxes, 1988–2003, Global Biogeochemical Cycles, 20, GB1002, doi:10.1029/2004GB002439, 2006.

Bakker, D. C. E., Pfeil, B., Landa, C. S., Metzl, N., O'Brien, K. M., Olsen, A., Smith, K., Cosca, C., Harasawa, S., Jones, S. D., Nakaoka, S.-I., Nojiri, Y., Schuster, U., Steinhoff, T., Sweeney, C., Takahashi, T., Tilbrook, B., Wada, C., Wanninkhof, R., Alin, S. R., Balestrini, C. F., Barbero, L., Bates, N. R., Bianchi, A. A., Bonou, F., Boutin, J., Bozec, Y., Burger, E. F., Cai, W.-J., Castle, R. D., Chen, L., Chierici, M., Currie, K., Evans, W., Featherstone, C., Feely, R. A., Fransson, A., Goyet, C., Greenwood, N., Gregor, L., Hankin, S., Hardman-Mountford, N. J., Harlay, J., Hauck, J., Hoppema, M., Humphreys, M. P., Hunt, C. W., Huss, B., Ibánhez, J. S. P., Johannessen, T., Keeling, R., Kitidis, V., Körtzinger, A., Kozyr, A., Krasakopoulou, E., Kuwata, A., Landschützer, P., Lauvset, S. K., Lefèvre, N., Lo Monaco, C., Manke, A., Mathis, J. T., Merlivat, L., Millero, F. J., Monteiro, P. M. S., Munro, D. R., Murata, A., Newberger, T., Omar, A. M., Ono, T., Paterson, K., Pearce, D., Pierrot, D., Robbins, L. L., Saito, S., Salisbury, J., Schlitzer, R., Schneider, B., Schweitzer, R., Sieger, R., Skjelvan, I., Sullivan, K. F., Sutherland, S. C., Sutton, A. J., Tadokoro, K., Telszewski, M., Tuma, M., van Heuven, S. M. A. C., Vandemark, D., Ward, B., Watson, A. J., and Xu, S.: A multi-decade record of high-quality fCO$_2$ data in version 3 of the Surface Ocean CO_2 Atlas (SOCAT), Earth System Science Data, 8, 383–413, doi:10.5194/essd-8-383-2016, 2016.

Bakker, D. C. E., Alin, S. R., Bates, N., Becker, M., Castaño-Primo, R., Cosca, C. E., Cronin, M., Kadono, K., Kozyr, A., Lauvset, S. K., Metzl, N., Munro, D. R., Nakaoka, S., O'Brien, K. M., Ólafsson, J., Olsen, A., Pfeil, B., Pierrot, D., Smith, K., Sutton, A. J., Takahashi, T., Tilbrook, B., Wanninkhof, R., Andersson, A., Atamanchuk, D., Benoit-Cattin, A., Bott, R., Burger, E. F., Cai, W.-J., Cantoni, C., Collins, A., Corredor, J. E., Cronin, M. F., Cross, J. N., Currie, K. I., De Carlo, E. H., DeGrandpre, M. D., Dietrich, C., Emerson, S., Enright, M. P., Evans, W., Feely, R. A., García-Ibáñez, M. I., Gkritzalis, T., Glockzin, M., Hales, B., Hartman, S. E., Hashida, G., Herndon, J., Howden, S. D., Humphreys, M. P., Hunt, C. W., Jones, S. D., Kim, S., Kitidis, V., Landa, C. S., Landschützer, P., Lebon, G. T., Lefèvre, N., Lo Monaco, C., Luchetta, A., Maenner Jones, S., Manke, A. B., Manzello, D., Mears, P., Mickett, J., Monacci, N. M., Morell, J. M., Musielewicz, S., Newberger, T., Newton, J., Noakes, S., Noh, J.-H., Nojiri, Y., Ohman, M., Ólafsdóttir, S. R., Omar, A. M., Ono, T., Osborne, J., Plueddemann, A. J., Rehder, G., Sabine, C. L., Salisbury, J. E., Schlitzer, R., Send, U., Skjelvan, I., Sparnocchia, S., Steinhoff, T., Sullivan, K. F., Sutherland, S. C., Sweeney, C., Tadokoro, K., Tanhua, T., Telszewski, M., Tomlinson, M., Tribollet, A., Trull, T., Vandemark, D., Wada, C., Wallace, D. W. R., Weller, R. A., and Woosley, R. J.: Surface Ocean CO2 Atlas Database Version 2020 (SOCATv2020) (NCEI Accession 0210711), NOAA National Centers for Environmental Information. Available at: https://doi.org/10.25921/4xkx-ss49. Last accessed: 2020-06-26, 2020.

Bousquet, P., Peylin, P., Ciais, P., Le Quéré, C., Friedlingstein, P., and Tans, P. P.: Regional changes in carbon dioxide fluxes of land and oceans since 1980, Science, 290, 1342–1346, 2000.

Carroll, D., Menemenlis, D., Adkins, J. F., Bowman, K. W., Brix, H., and Dutkiewicz, S., e. a.: The ECCO-Darwin data-assimilative global ocean biogeochemistry model: Estimates of seasonal to multidecadal surface ocean pCO2 and air-sea CO2 flux, Journal of Advances in Modeling Earth Systems, 12, e2019MS001 888, doi:10.1029/2019MS001888, 2020.

Conkright, M., Locarnini, R. A., Garcia, H., O'Brien, T., Boyer, T., Stephens, C., and Antonov, J.: World Ocean Atlas 2001: Objective Analyses, Data Statistics, and Figures, CD-ROM Documentation. National Oceanographic Data Center, Silver Spring, MD, 17 pp., 2002.

Conway, T., Tans, P., Waterman, L., Thoning, K., Kitzis, D., Masarie, K., and Zhang, N.: Evidence for interannual variability of the carbon cycle from the national oceanic and atmospheric administration climate monitoring and diagnostics laboratory global air sampling network, J. Geophys. Res., 99, 22,831–22,855, 1994.

de Boyer Montégut, C., Madec, G., Fischer, A. S., Lazar, A., and Iudicone, D.: Mixed layer depth over the global ocean: an examination of profile data and a profile-based climatology, JGR, 109, C12 003, doi:10.1029/2004JC002378, 2004.

Denvil-Sommer, A., Gehlen, M., Vrac, M., and Mejia, C.: LSCE-FFNN-v1: a two-step neural network model for the reconstruction of surface ocean pCO2 over the global ocean, Geosci. Model Dev., 12, 2091–2105, doi:10.5194/gmd-12-2091-2019, 2019.

DeVries, T.: Atmospheric CO2 and sea surface temperature variability cannot explain recent decadal variability of the ocean CO2 sink, Geophysical Research Letters, 49, e2021GL096 018, doi:10.1029/2021GL096018, 2022.

DeVries, T., Le Quéré, C., Andrews, O., Berthet, S., Hauck, J., Ilyina, T., Landschützer, P., Lenton, A., Lima, I. D., Nowick, M., Schwinger, J., and Séférian, R.: Decadal trends in the ocean carbon sink, PNAS, 116, 11 646–11 651, doi:10.1073/pnas.1900371116, 2019.

Feely, R. A., Wanninkhof, R., Takahashi, T., and Tans, P.: Influence of El Niño on the equatorial Pacific contribution to atmospheric CO_2 accumulation, Nature, 398, 597–601, 1999.

Francey, R., Steele, L., Spencer, D., Langenfelds, R., Law, R., Krummel, P., Fraser, P., Etheridge, D., Derek, N., Coram, S., Cooper, L., Allison, C., Porter, L., and Baly, S.: The CSIRO (Australia) measurement of greenhouse gases in the global atmosphere, Report of the 11th WMO/IAEA Meeting of Experts on Carbon Dioxide Concentration and Related Tracer Measurement Techniques, Tokyo, Japan, September 2001, S.Toru and S. Kazuto (editors), World Meteorological Organization Global Atmosphere Watch, 97-111, 2003.

Friedlingstein, P., O'Sullivan, M., Jones, M. W., Andrew, R. M., Hauck, J., Olsen, A., Peters, G. P., Peters, W., Pongratz, J., Sitch, S., Le Quéré, C., Canadell, J. G., Ciais, P., Jackson, R. B., Alin, S., Aragão, L. E. O. C., Arneth, A., Arora, V., Bates, N. R., Becker, M., Benoit-Cattin, A., Bittig, H. C., Bopp, L., Bultan, S., Chandra, N., Chevallier, F., Chini, L. P., Evans, W., Florentie, L., Forster, P. M., Gasser, T., Gehlen, M., Gilfillan, D., Gkritzalis, T., Gregor, L., Gruber, N., Harris, I., Hartung, K., Haverd, V., Houghton, R. A., Ilyina, T., Jain, A. K., Joetzjer, E., Kadono, K., Kato, E., Kitidis, V., Korsbakken, J. I., Landschützer, P., Lefèvre, N., Lenton, A., Lienert, S., Liu, Z., Lombardozzi, D., Marland, G., Metzl, N., Munro, D. R., Nabel, J. E. M. S., Nakaoka, S.-I., Niwa, Y., O'Brien, K., Ono, T., Palmer, P. I., Pierrot, D., Poulter, B., Resplandy, L., Robertson, E., Rödenbeck, C., Schwinger, J., Séférian, R., Skjelvan, I., Smith, A. J. P., Sutton, A. J., Tanhua, T., Tans, P. P., Tian, H., Tilbrook, B., van der Werf, G., Vuichard, N., Walker, A. P., Wanninkhof, R., Watson, A. J., Willis, D., Wiltshire, A. J., Yuan, W., Yue, X., and Zaehle, S.: Global Carbon Budget 2020, Earth System Science Data, 12, 3269–3340, doi:10.5194/essd-12-3269-2020, 2020.

Garcia, H. E., Locarnini, R. A., Boyer, T. P., and Antonov, J. I.: World Ocean Atlas 2005, Volume 4: Nutrients (phosphate, nitrate, silicate), S. Levitus, Ed. NOAA Atlas NESDIS 64, U.S. Government Printing Office, Washington, D.C., 396 pp., 2006.

Gloege, L., McKinley, G. A., Landschützer, P., Fay, A. R., Frölicher, T. L., and Fyfe, J. C., e. a.: Quantifying errors in observationally-based estimates of ocean carbon sink variability, Global Biogeochemical Cycles, 35, e2020GB006 788, doi:10.1029/2020GB006788, 2021.

Good, S. A., Martin, M. J., and Rayner, N. A.: EN4: quality controlled ocean temperature and salinity profiles and monthly objective analyses with uncertainty estimates, Journal of Geophysical Research: Oceans, 118, 6704–6716, doi:10.1002/2013JC009067, 2013.

Gregor, L., Lebehot, A. D., Kok, S., and Scheel Monteiro, P. M.: A comparative assessment of the uncertainties of global surface ocean CO_2 estimates using a machine-learning ensemble (CSIR-ML6 version 2019a) – have we hit the wall?, Geoscientific Model Development, 12, 5113–5136, doi:10.5194/gmd-12-5113-2019, https://gmd.copernicus.org/articles/12/5113/2019/, 2019.

Gruber, N., Clement, D., Carter, B. R., Feely, R. A., van Heuven, S., Hoppema, M., Ishii, M., Key, R. M., Kozyr, A., Lauvset, S. K., Lo Monaco, C., Mathis, J. T., Murata, A., Olsen, A., Perez, F. F., Sabine, C. L., Tanhua, T., and Wanninkhof, R.: The oceanic sink for anthropogenic CO2 from 1994 to 2007, Science, 363, 1193–1199, doi:10.1126/science.aau5153, 2019.

Hauck, J., Völker, C., Wang, T., Hoppema, M., Losch, M., and Wolf-Gladrow, D. A.: Seasonally different carbon flux changes in the Southern Ocean in response to the southern annular mode, Global Biogeochemical Cycles, 27, 1236–1245, doi:10.1002/2013GB004600, 2013.

Hauck, J., Zeising, M., Quéré, C. L., Gruber, N., Bakker, D. C. E., Bopp, L., Chau, T. T. T., Gürses, Ö., Ilyina, T., Landschützer, P., Lenton, A., Resplandy, L., Rödenbeck, C., Schwinger, J., and Séférian, R.: Consistency and challenges in the ocean carbon sink estimate for the Global Carbon Budget, Frontiers in Marine Science, 7, 852, doi:10.3389/fmars.2020.571720, 2020.

Hirt, C. and Rexer, M.: Earth2014: 1 arc-min shape, topography, bedrock and ice-sheet models - available as gridded data and degree-10,800 spherical harmonics, International Journal of Applied Earth Observation and Geoinformation, 39, 103–112, doi:10.1016/j.jag.2015.03.001, 2015.

Huang, B., Thorne, P. W., Banzon, V. F., Boyer, T., Chepurin, G., Lawrimore, J. H., Menne, M. J., Smith, T. M., Vose, R. S., and Zhang, H.-M.: NOAA Extended Reconstructed Sea Surface Temperature (ERSST), Version 5., NOAA National Centers for Environmental Information. doi:10.7289/V5T72FNM, accessed on 2020-06-26 from ftp://ftp.cdc.noaa.gov/Datasets/noaa.ersst.v5/sst.mnmean.nc, 2017.

Iida, Y., Kojima, A., Takatani, Y., Nakano, T., Midorikawa, T., and Ishii, M.: Trends in pCO$_2$ and sea-air CO$_2$ flux over the global open oceans for the last two decades., Journal of Oceanography, DOI 10.1007/s10872-015-0306-4, 2015.

Iida, Y., Takatani, Y., Kojima, A., and Ishii, M.: Global trends of ocean CO2 sink and ocean acidification: an observation-based reconstruction of surface ocean inorganic carbon variables, Journal of Oceanography, doi:10.1007/s10872-020-00571-5, 2020.

IPCC: Climate Change 2013: The Physical Science Basis. Contribution of Working Group I to the Fifth Assessment Report of the Intergovernmental Panel on Climate Change, [Stocker, T.F., D. Qin, G.-K. Plattner, M. Tignor, S.K. Allen, J. Boschung, A. Nauels, Y. Xia, V. Bex and P.M. Midgley (eds.)]. Cambridge University Press, Cambridge, United Kingdom and New York, NY, USA, 1535 pp., 2013.

Jacobson, A. R., Fletcher, S. E. M., Gruber, N., Sarmiento, J. L., and Gloor, M.: A joint atmosphere-ocean inversion for surface fluxes of carbon dioxide: 2. Regional results, Glob. Biogeochem. Cycles, 21, GB1020, doi:10.1029/2006GB002703, 2007.

Jones, S. D., Quéré, C. L., Rödenbeck, C., Manning, A. C., and Olsen, A.: A statistical gap-filling method to interpolate global monthly surface ocean carbon dioxide data, J. Adv. Model. Earth Syst., 07, doi:10.1002/2014MS000 416, 2015.

Kalnay, E., Kanamitsu, M., Kistler, R., Collins, W., Deaven, D., Gandin, L., Iredell, M., Saha, S., White, G., Woollen, J., Zhu, Y., Chelliah, M., Ebisuzaki, W., Higgins, W., Janowiak, J., Mo, K. C., Ropelewski, C., Wang, J., Leetmaa, A., Reynolds, R., Jenne, R., and Joseph, D.: The NCEP/NCAR 40-year reanalysis project, Bull. Am. Met. Soc., 77, 437–471, 1996.

Keeling, C. D.: The Influence of Mauna Loa Observatory on the Development of Atmospheric CO2 Research, in "Mauna Loa Observatory: a 20th anniversary report", Ed. John Miller, Silver Spring, Md.: U.S. Dept. of Commerce, National Oceanic and Atmospheric Administration, Environmental Research Laboratories, pp. 35-54, 1978.

Landschützer, P., Gruber, N., Bakker, D. C. E., Schuster, U., Nakaoka, S., Payne, M. R., Sasse, T., and Zeng, J.: A neural network-based estimate of the seasonal to inter-annual variability of the Atlantic Ocean carbon sink, Biogeosciences, 10, 7793–7815, 2013.

Landschützer, P., Gruber, N., and Bakker, D. C. E.: Decadal variations and trends of the global ocean carbon sink, Global Biogeochem. Cycles, 30, 1396–1417, doi:10.1002/2015GB005359, 2016.

Laws, E., Falkowski, P., Smith, W., Ducklow, H., and Mccarthy, J.: Temperature effects on export production in the open ocean, Global Biogeochemical Cycles, 14, 1231–1246, doi:10.1029/1999GB001229, 2000.

Le Quéré, C., Orr, J. C., Monfray, P., and Aumont, O.: Interannual variability of the oceanic sink of CO2 from 1979 through 1997, Global Biogeochemical Cycles, 14, 1247–1265, 2000.

Le Quéré, C., Rödenbeck, C., Buitenhuis, E. T., Conway, T. J., Langenfelds, R., Gomez, A., Labuschagne, C., Ramonet, M., Nakazawa, T., Metzl, N., Gillett, N., and Heimann, M.: Saturation of the Southern Ocean CO2 Sink Due to Recent Climate Change, Science, 316, 1735–1738, doi:10.1126/science.1136188, 2007.

Lee, K., Tong, L. T., Millero, F. J., Sabine, C. L., Dickson, A. G., Goyet, C., Park, G.-H., Wanninkhof, R., Feely, R. A., and Key, R. M.: Global relationships of total alkalinity with salinity and temperature in surface waters of the world's oceans, Geophys Research Letters, 33, L19 605, doi:10.1029/2006GL027207, 2006.

Majkut, J. D., Sarmiento, J. L., and Rodgers, K. B.: A growing oceanic carbon uptake: Results from an inversion study of surface pCO_2 data, Global Biogeochem. Cycles, 28, 335–351, 2014.

Maritorena, S., d'Andon, O. H. F., Mangin, A., and Siegel, D. A.: Merged satellite ocean color data products using a bio-optical model: Characteristics, benefits and issues, Remote Sensing of Environment, 114, 1791–1804, doi:10.1016/j.rse.2010.04.002, 2010.

Naegler, T.: Reconciliation of excess ^{14}C-constrained global CO_2 piston velocity estimates, Tellus, 61B, 372–384, 2009.

Nakaoka, S., Telszewski, M., Nojiri, Y., Yasunaka, S., Miyazaki, C., Mukai, H., and Usui, N.: Estimating temporal and spatial variation of ocean surface pCO_2 in the North Pacific using a self-organizing map neural network technique, Biogeosciences, 10, 6093–6106, 2013.

Newsam, G. N. and Enting, I. G.: Inverse problems in atmospheric constituent studies: I. Determination of surface sources under a diffusive transport approximation, Inverse Problems, 4, 1037–1054, 1988.

Orr, J. C. and Epitalon, J.-M.: Improved routines to model the ocean carbonate system: mocsy 2.0, Geoscientific Model Development, 8, 485–499, doi:10.5194/gmd-8-485-2015, https://www.geosci-model-dev.net/8/485/2015/, 2015.

Peylin, P., Law, R. M., Gurney, K. R., Chevallier, F., Jacobson, A. R., Maki, T., Niwa, Y., Patra, P. K., Peters, W., Rayner, P. J., Rödenbeck, C., van der Laan-Luijkx, I. T., and Zhang, X.: Global atmospheric carbon budget: results from an ensemble of atmospheric CO_2 inversions, Biogeosciences, 10, 6699–6720, 2013.

Rayner, P., Enting, I., Francey, R., and Langenfelds, R.: Reconstructing the recent carbon cycle from atmospheric CO_2, $\delta^{13}CO_2$ and O_2/N_2 observations, Tellus, 51B, 213–232, 1999.

Resplandy, L., Keeling, R. F., Rödenbeck, C., Stephens, B. B., Khatiwala, S., Rodgers, K. B., Long, M. C., Bopp, L., and Tans, P. P.: Revision of global carbon fluxes based on a reassessment of oceanic and riverine carbon transport, Nat. Geosci., 11, 504–509, doi:10.1038/s41561-018-0151-3, 2018.

Robertson, J. E. and Watson, A. J.: Thermal skin effect of the surface ocean and its implications for CO2 uptake, Nature, 358, 738–740, 1992.

Rödenbeck, C.: Estimating CO_2 sources and sinks from atmospheric mixing ratio measurements using a global inversion of atmospheric transport, Tech. Rep. 6, Max Planck Institute for Biogeochemistry, Jena, Germany, 2005.

Rödenbeck, C., Houweling, S., Gloor, M., and Heimann, M.: CO_2 flux history 1982-2001 inferred from atmospheric data using a global inversion of atmospheric transport, Atmospheric Chemistry and Physics, 3, 1919–1964, 2003.

Rödenbeck, C., Keeling, R. F., Bakker, D. C. E., Metzl, N., Olsen, A., Sabine, C., and Heimann, M.: Global surface-ocean pCO_2 and sea–air CO_2 flux variability from an observation-driven ocean mixed-layer scheme, Ocean Science, 9, 193–216, doi:10.5194/os-9-193-2013, http://www.ocean-sci.net/9/193/2013/, 2013.

Rödenbeck, C., Bakker, D. C. E., Metzl, N., Olsen, A., Sabine, C., Cassar, N., Reum, F., Keeling, R. F., and Heimann, M.: Interannual sea–air CO_2 flux variability from an observation-driven ocean mixed-layer scheme, Biogeosciences, 11, 4599–4613, 2014.

Rödenbeck, C., Bakker, D. C. E., Gruber, N., Iida, Y., Jacobson, A. R., Jones, S., Landschützer, P., Metzl, N., Nakaoka, S., Olsen, A., Park, G.-H., Peylin, P., Rodgers, K. B., Sasse, T. P., Schuster, U., Shutler, J. D., Valsala, V., Wanninkhof, R., and Zeng, J.: Data-based estimates of the ocean carbon sink variability - first results of the Surface Ocean pCO_2 Mapping intercomparison (SOCOM), Biogeosciences, 12, 7251–7278, doi:10.5194/bg-12-7251-2015, https://www.biogeosciences.net/12/7251/2015/, 2015.

5 Rödenbeck, C., Zaehle, S., Keeling, R., and Heimann, M.: History of El Nino impacts on the global carbon cycle 1957-2016: A quantification from atmospheric CO2 data, Philosophical Transactions of the Royal Society B: Biological Sciences, 373, 20170303, doi:10.1098/rstb.2017.0303, 2018a.

Rödenbeck, C., Zaehle, S., Keeling, R., and Heimann, M.: How does the terrestrial carbon exchange respond to interannual climatic variations? A quantification based on atmospheric CO_2 data, Biogeosciences, 15, 1–18, doi:10.5194/bg-15-1-2018, 2018b.

10 Sarmiento, J. L. and Gruber, N.: Ocean Biogeochemical Dynamics, Princeton Univ. Press, 2006.

Takahashi, T., Sutherland, S. C., Wanninkhof, R., Sweeney, C., Feely, R. A., Chipman, D. W., Hales, B., Friederich, G., Chavez, F., Sabine, C., Watson, A., Bakker, D. C. E., Schuster, U., Metzl, N., Yoshikawa-Inoue, H., Ishii, M., Midorikawa, T., Nojiri, Y., Kortzinger, A., Steinhoff, T., Hoppema, M., Olafsson, J., Arnarson, T. S., Tillbrook, B., Johannessen, T., Olsen, A., Bellerby, R., Wong, C. S., Delille, B., Bates, N. R., and de Baar, H. J. W.: Climatological mean and decadal change in surface ocean pCO_2 and net sea-air CO_2 flux over the

15 global oceans, Deep-Sea Res. II, 56, 554–577, 2009.

Thacker, W. C.: Regression-based estimates of the rate of accumulation of anthropogenic CO2 in the ocean: A fresh look, Marine Chemistry, 132-133, 44–55, doi:10.1016/j.marchem.2012.02.004, 2012.

Titchner, H. A. and Rayner, N. A.: The Met Office Hadley Centre sea ice and sea surface temperature data set, version 2: 1. Sea ice concentrations, J. Geophys. Res. Atmos., 119, 2864–2889, doi:10.1002/2013JD020316, 2014.

20 Tsujino, H., Urakawa, S., Nakano, H., Small, R. J., Kim, W. M., Yeager, S. G., Danabasoglu, G., Suzuki, T., Bamber, J. L., Bentsen, M., Boening, C., Bozec, A., Chassignet, E., Curchitser, E., Dias, F. B., Durack, P. J., Griffies, S. M., Harada, Y., Ilicak, M., Josey, S., Kobayashi, C., Kobayashi, S., Komuro, Y., Large, W. G., Le Sommer, J., Marsland, S., Masina, S., Scheinert, M., Tomita, H., Valdivieso, M., and Yamazaki, D.: input4MIPs.CMIP6.OMIP.MRI, doi:10.22033/ESGF/input4MIPs.10460, 2018.

Valsala, K. V. and Maksyutov, S.: Simulation and assimilation of global ocean pCO2 and air-sea CO2 fluxes using ship observations of

25 surface ocean pCO2 in a simplified Biogeochemical offline model, Tellus, 62B, 821–840, 2010.

Wanninkhof, R.: Relationship between wind speed and gas exchange over the ocean, Journal of Geophysical Research-Oceans, 97, 7373–7382, 1992.

Watson, A. J., Schuster, U., Bakker, D. C. E., Bates, N. R., Corbiére, A., González-Dávila, M., Friedrich, T., Hauck, J., Heinze, C., Johannessen, T., Körtzinger, A., Metzl, N., Olafsson, J., Olsen, A., Oschlies, A., Padin, X. A., Pfeil, B., Santana-Casiano, J. M., Steinhoff,

30 T., Telszewski, M., Rios, A. F., Wallace, D. W. R., and Wanninkhof, R.: Tracking the Variable North Atlantic Sink for Atmospheric CO_2, Science, 326, 1391–1393, 2009.

Watson, A. J., Schuster, U., Shutler, J. D., Holding, T., Ashton, I. G. C., Landschützer, P., Woolf, D. K., and Goddijn-Murphy, L.: Revised estimates of ocean-atmosphere CO2 flux are consistent with ocean carbon inventory, Nature Communications, 11, 4422, doi:10.1038/s41467-020-18203-3, 2020.

35 Weiss, R.: Carbon dioxide in water and seawater: the solubility of a non-ideal gas., Marine Chemistry, 2, 203–205, 1974.

Wolter, K. and Timlin, M.: Monitoring ENSO in COADS with a seasonally adjusted principal component index, Proc. of the 17th Climate Diagnostics Workshop, Norman, OK, NOAA/N MC/CAC, NSSL, Oklahoma Clim. Survey, CIMMS and the School of Meteor., Univ. of Oklahoma, pp. 52–57, 1993.

Woolf, D. K., Land, P. E., Shutler, J. D., Goddijn-Murphy, L. M., and Donlon, C. J.: On the calculation of air-sea fluxes of CO2 in the presence of temperature and salinity gradients, J. Geophys. Res. Oceans, 121, 1229–1248, 2016.

Yu, L. and Weller, R. A.: Objectively Analyzed air-sea heat Fluxes (OAFlux) for the global oceans, Bull. Am. Met. Soc., 88, 527–539, 2007.

Zeng, J., Nojiri, Y., Nakaoka, S., Nakajima, H., and Shirai, T.: Surface ocean CO_2 in 1990-2011 modelled using a feed-forward neural network, Geoscience Data Journal, 2, 47–51, 2015.

Table 1. Input data sets

Quantity	Data set	Reference	Pre-treatment, original resolution, remarks	Used for
$p\text{CO}_2$	SOCATv2021	Bakker et al. (2016, 2020), http://www.socat.info/	Data are used having WOCE-flag = 2 and valid fields for fugacity, temperature, and salinity. Values below 200 µatm or above 600 µatm have been excluded as being local compared to the grid cells. Values have been transferred from fugacity to partial pressure by dividing by 0.996.	Main constraint
Ocean fraction	Earth2014	Hirt and Rexer (2015), http://ddfe.curtin.edu.au/models/ Earth2014/data_1min/masks/ MSK2014_landtypes.1min.geod.bin, accessed 2020-11-12	$1' \times 1'$; using land type 2 ("ocean bathymetry")	Param.
SST	Hadley EN.4.2.1 (g10)	Good et al. (2013)		Param., Expl. var.
Ice-free fraction	HadISST 2.2.0.0.	Titchner and Rayner (2014), https://www.metoffice.gov.uk/hadobs/ hadisst2/, accessed 2020-06-05	$1° \times 1°$, monthly	Param.
MLD	LOCEAN	de Boyer Montégut et al. (2004)	$2° \times 2°$, monthly climatology; using "temperature criterion"	Param.
u	JRA55-do v1.5.0	Tsujino et al. (2018)	$0.5625° \times 0.5625°$, 3-hourly	Param., Expl. var.
Sea-level press.	JRA55-do v1.5.0	Tsujino et al. (2018)	$0.5625° \times 0.5625°$, 3-hourly	Param.
Atm. $X\text{CO}_2$	Jena CarboScope sEXTALL_v2021	Rödenbeck et al. (2018b)	$5° \times 3.83°$, daily; atmospheric inversion	Param.
Alk	CDIAC	Lee et al. (2006)	$1° \times 1°$, monthly climatology	Param.
Salinity	WOA01	Conkright et al. (2002)	$1° \times 1°$, monthly climatology; via Lee et al. (2006)	Param.
PO_4, Si	WOA05	Garcia et al. (2006)	$1° \times 1°$, monthly	Param.
Sea–air CO_2 flux	OCIM	DeVries (2022)	$2° \times 2°$, monthly; using "total flux", decadally smoothed	Prior

Glossary: LOCEAN = Laboratoire d'océanographie et du climat: expérimentations et approches numériques; NCEP = National Centers for Environmental Prediction; SOCAT = Surface Ocean CO_2 Atlas; WOCE = World Ocean Circulation Experiment; WOA = World Ocean Atlas; Param. = Parameterizations; Expl. var. = Explanatory variable

Table 2. Mapping runs used in this study. The main results are given in bold; the other runs are used to assess uncertainty ("uncertainty cases", Sect. 2.2), to illustrate specific points of discussion ("test cases", Sect. 2.2), or to assess predictive skill ("cross-validation", Sect. 2.3).

Run	Representation of f_{int}	Special feature (if any)	CarboScope RunID
Pre-mapping	Eq. (3)	Lin. of C chem. around $p_a\text{CO}_2$	ocP_v2021
Zero-prior expl. interann. $p\text{CO}_2$ map.	Eq. (1)		ocZE_v2021
Explicitly interannual $p\text{CO}_2$ mapping	Eq. (2)		ocE_v2021
Expl. interann. map. (cross-validation)	Eq. (2)	No $p\text{CO}_2$ data 1995–1999	ocE_CrossVal5yr1995_v2021
Multi-linear $p\text{CO}_2$ regression	Eq. (3)		ocR_v2021
Multi-linear regr. (uncertainty case RegrSSTNOAA)	Eq. (3)	SST from NOAA_ER	ocR_RegrSSTNOAA_v2021
Multi-linear regr. (uncertainty case RegrU2NCEP)	Eq. (3)	u^2 from NCEP reanalysis	ocR_RegrU2NCEP_v2021
Multi-linear regr. (uncertainty case RegrAdddSSTdt2)	Eq. (3)	Added $(\text{d}SST/\text{d}t)^2$ regression term	ocR_RegrAdddSSTdt2_v2021
Multi-linear regr. (uncertainty case RegrAddU4)	Eq. (3)	Added u^4 regression term	ocR_RegrAddU4_v2021
Multi-linear regr. (uncertainty case RegrAddpaCO2)	Eq. (3)	Added $p_a\text{CO}_2$ regression term	ocR_RegrAddpaCO2_v2021
Multi-linear regr. (uncertainty case RegrLoose)	Eq. (3)	4-fold a-priori sigma of regr. terms	ocR_RegrLoose_v2021
Multi-linear regr. (uncertainty case RegrShort)	Eq. (3)	3-fold shorter a-pr. correlation length	ocR_RegrShort_v2021
Multi-linear regr. (uncertainty case RegrNoDecad)	Eq. (3)	No decadal variab. in explanat. var.	ocR_RegrNoDecad_v2021
Multi-linear regr. (uncertainty case MLDq2)	Eq. (3)	Halved mixed-layer depth	ocR_MLDq2_v2021
Multi-linear regr. (uncertainty case MLDx2)	Eq. (3)	Doubled mixed-layer depth	ocR_MLDx2_v2021
Multi-linear regr. (uncertainty case GasexLow)	Eq. (3)	Reduced gas transfer velocity	ocR_GasexLow_v2021
Multi-linear regr. (uncertainty case GasexHigh)	Eq. (3)	Enhanced gas transfer velocity	ocR_GasexHigh_v2021
Multi-linear regr. (uncertainty case GasexU1)	Eq. (3)	Gas transfer velocity prop. to $|u|$	ocR_GasexU1_v2021
Multi-linear regr. (uncertainty case GasexU3)	Eq. (3)	Gas transfer velocity prop. to $|u|^3$	ocR_GasexU3_v2021
Multi-linear regr. (test case RegrOnlySST)	Eq. (3)	SST regression term only	ocR_RegrOnlySST_v2021
Multi-linear regr. (test case RegrOnlydSSTdt)	Eq. (3)	dSST/dt regression term only	ocR_RegrOnlydSSTdt_v2021
Multi-linear regr. (test case RegrOnlyU2)	Eq. (3)	u^2 regression term only	ocR_RegrOnlyU2_v2021
Multi-linear regr. (test case RegrAddChl_98r19)	Eq. (3)	Added Chl-a regression term[a]	ocR_RegrAddChl_98r19_v2021
Multi-linear regr. (test case 98r19)	Eq. (3)	Regr. 1998–2019 only	ocR_98r19_v2021
Multi-linear regr. (test case RegrHeat_85r09)	Eq. (3)	Repl. dSST/dt by the sea–air heat flux[a]	ocR_RegrHeat_85r09_v2021
Multi-linear regr. (test case 85r09)	Eq. (3)	Regr. 1985–2009 only	ocR_85r09_v2021
Multi-linear regr. (test case RegrCurl_88r18)	Eq. (3)	Replacing u^2 by windstress curl[a]	ocR_RegrCurl_88r18_v2021
Multi-linear regr. (test case 88r18)	Eq. (3)	Regr. 1988–2018 only	ocR_88r18_v2021
Multi-linear regr. (cross-validation)	Eq. (3)	No $p\text{CO}_2$ data 1985–1989	ocR_CrossVal5yr1985_v2021
Multi-linear regr. (cross-validation)	Eq. (3)	No $p\text{CO}_2$ data 1990–1994	ocR_CrossVal5yr1990_v2021
Multi-linear regr. (cross-validation)	Eq. (3)	No $p\text{CO}_2$ data 1995–1999	ocR_CrossVal5yr1995_v2021
Multi-linear regr. (cross-validation)	Eq. (3)	No $p\text{CO}_2$ data 2000–2004	ocR_CrossVal5yr2000_v2021
Multi-linear regr. (cross-validation)	Eq. (3)	No $p\text{CO}_2$ data 2005–2009	ocR_CrossVal5yr2005_v2021
Multi-linear regr. (cross-validation)	Eq. (3)	No $p\text{CO}_2$ data 2010–2014	ocR_CrossVal5yr2010_v2021
Hybrid $p\text{CO}_2$ mapping	Eq. (4)		oc_v2021
Hybrid mapping (uncertainty case RegrSSTNOAA)	Eq. (4)	SST from NOAA_ER	oc_RegrSSTNOAA_v2021
Hybrid mapping (uncertainty case RegrU2NCEP)	Eq. (4)	u^2 from NCEP reanalysis	oc_RegrU2NCEP_v2021
Hybrid mapping (uncertainty case RegrLoose)	Eq. (4)	4-fold a-priori sigma of regr. terms	oc_RegrLoose_v2021
Hybrid mapping (uncertainty case RegrShort)	Eq. (4)	3-fold shorter a-pr. correlation length	oc_RegrShort_v2021
Hybrid mapping (uncertainty case RegrNoDecad)	Eq. (4)	No decadal variab. in explanat. var.	oc_RegrNoDecad_v2021
Hybrid mapping (uncertainty case MLDq2)	Eq. (4)	Halved mixed-layer depth	oc_MLDq2_v2021
Hybrid mapping (uncertainty case MLDx2)	Eq. (4)	Doubled mixed-layer depth	oc_MLDx2_v2021
Hybrid mapping (uncertainty case GasexLow)	Eq. (4)	Reduced gas transfer velocity	oc_GasexLow_v2021
Hybrid mapping (uncertainty case GasexHigh)	Eq. (4)	Enhanced gas transfer velocity	oc_GasexHigh_v2021
Hybrid mapping (uncertainty case GasexU1)	Eq. (4)	Gas transfer velocity prop. to $|u|$	oc_GasexU1_v2021
Hybrid mapping (uncertainty case GasexU3)	Eq. (4)	Gas transfer velocity prop. to $|u|^3$	oc_GasexU3_v2021
Hybrid mapping (cross-validation)	Eq. (4)	No $p\text{CO}_2$ data 1995–1999	oc_CrossVal5yr1995_v2021

[a] Regression run only over 1998–2019, 1985–2009, or 1988–2018, respectively

Table 3. The components of the contemporary net sea–air CO_2 flux ($F_{net} = F_{ant,ss} + F_{ant,ns} + F_{nat,ss} + F_{nat,ns} + F_{riv,ss} + F_{riv,ns}$) according to Hauck et al. (2020), and whether or not they are included in the individual estimates shown in Fig. 8, Fig. 9, and Fig. 10

Component of F_{net}	Definition	Included in			
		This study (F_{net})	OCIM "anthr."	GOBMs	Gruber et al. (2019)[2]
$F_{ant,ss}$	CO_2 uptake in direct response to the anthropogenic increase in atmospheric CO_2 hypothetically under constant pre-industrial circulation	X	X	X	X
$F_{ant,ns}$	modifications of $F_{ant,ss}$ due to anthropogenic climate change and natural climate variability	X	(X)[1]	X	X
$F_{nat,ss}$	steady-state natural fluxes under constant pre-industrial climate conditions; supposed to be zero in the global sum	X		X	
$F_{nat,ns}$	modifications of $F_{nat,ss}$ due to anthropogenic climate change and natural climate variability	X	(X)[1]	X	
$F_{riv,ss}$	steady-state outgassing of carbon transported into the ocean by rivers, minus the carbon sedimented at the ocean floor	X			
$F_{riv,ns}$	modifications of $F_{riv,ss}$ due to climate change and variability as well as anthropogenic land-use changes	X			

[1] for a mean ocean circulation over the industrial era, i.e., the variations are due to temperature and gas transfer velocity variations only; [2] mean 1994–2007 flux only
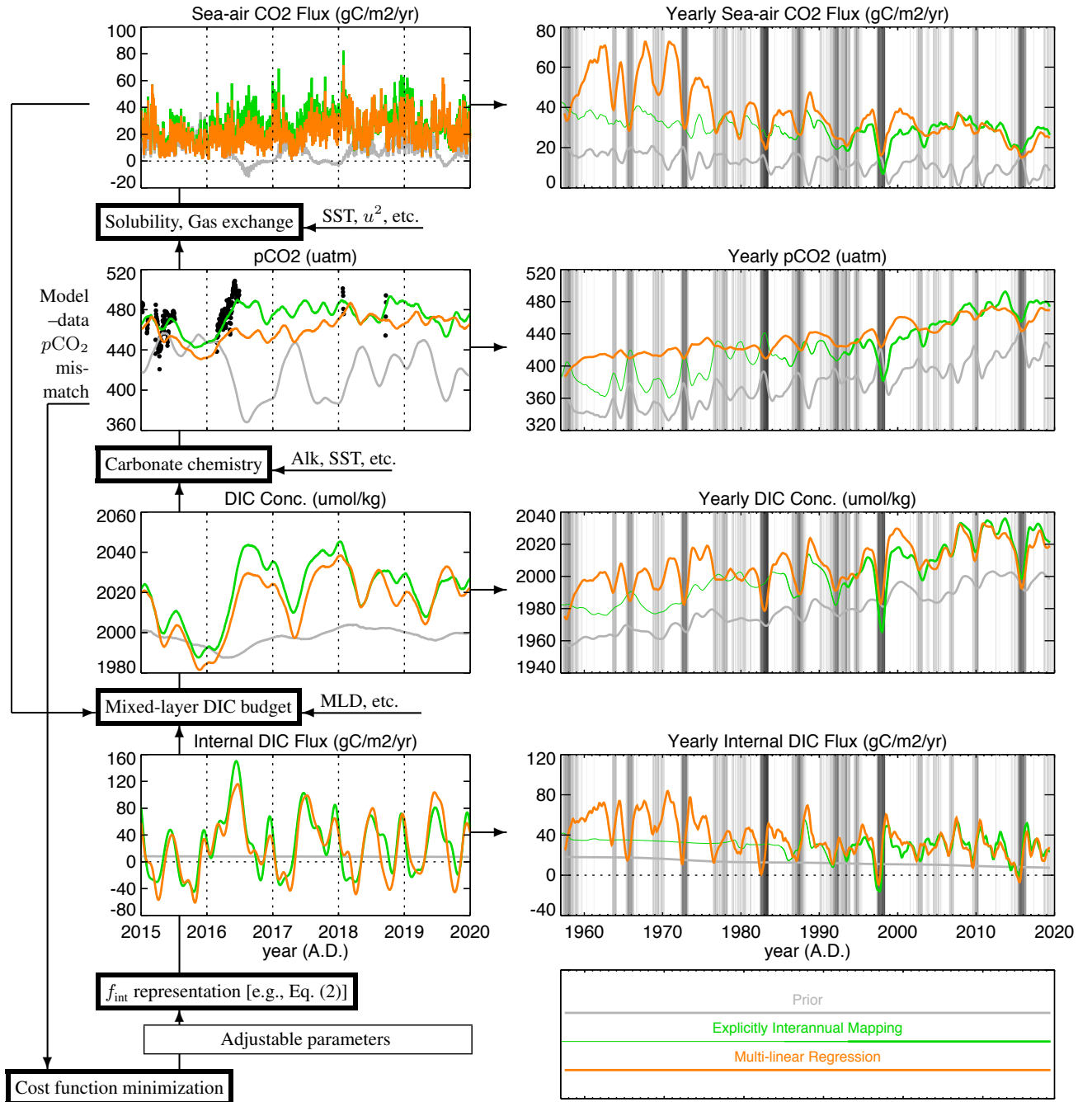
Figure 1. Illustration of the quantities involved in the mixed-layer scheme (time series panels), and the calculations done to connect them (thick-framed boxes). At the arrows on the right of each calculation box, we give its most important environmental input fields (see Table 1). The time series represent the example pixel enclosing the TAO140W mooring location (140° W, 2° N) in the tropical Pacific; they are taken from the results of this study but shown here for illustration only. *Left:* Quantities on the original daily time steps, plotted for 5 example years. *Right:* The same quantities displayed as smoothed yearly averages, which is the way all results will be shown in this paper. The background shading indicates the ENSO phase (Multivariate El Niño Index (MEI) by Wolter and Timlin, 1993).
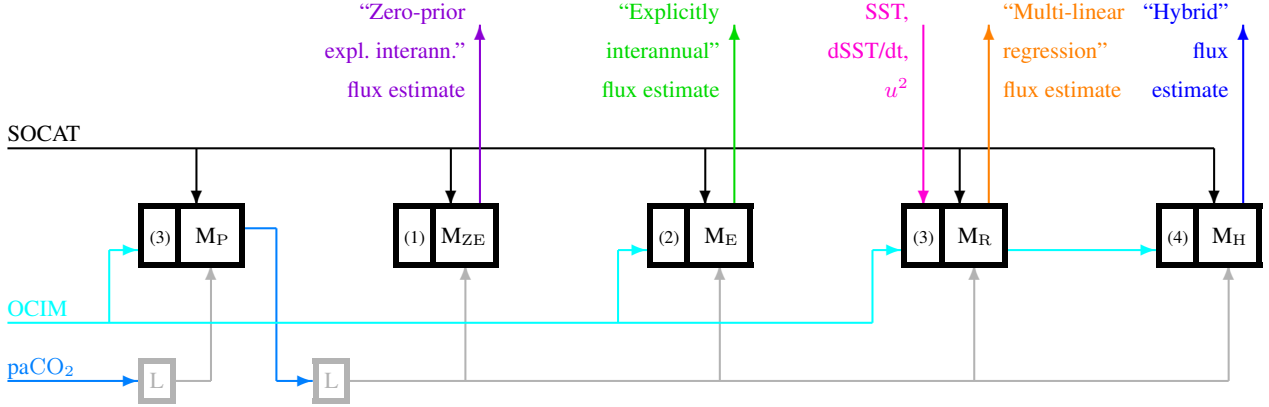
Figure 2. Information flow between the presented mapping runs. Thick-framed boxes denote calculations, with arrows denoting their input and output data sets (mostly spatio-temporal fields). The violet, green, orange, and blue arrows represent the spatio-temporal sea–air CO_2 fluxes estimated by our main mapping runs M_{ZE}, M_E, M_R, and M_H (these same 4 colors are also used in all line plots in this paper). All mapping runs use the SOCAT data base of pCO_2 measurements (point data, black) as their primary information source. The runs are algorithmically identical, except for the representation of the ocean-internal DIC sources/sinks (f_{int}) and the corresponding set of adjustable unknowns; this part of the mapping algorithm has therefore been represented explicitly as separate parts of the boxes at their left-hand sides, labelled by the respective equation number. Runs M_{ZE} and M_E are using the representations with explicit interannual degrees of freedom, either without f_{int} prior (Eq. (1)), or using the decadally smoothed OCIM result as f_{int} prior (cyan, Eq. (2)). Run M_R is using the representation involving regression terms (Eq. (3)), which requires the explanatory variables (magenta) as further input fields; it uses the same f_{int} prior as the run M_E. The representation of f_{int} in the "hybrid" run M_H again has explicit interannual degrees of freedom, but no long-term and seasonal degrees of freedom (Eq. (4)). Importantly, it uses the ocean-internal DIC sources/sinks estimated by the "multi-linear regression" M_R as its f_{int} prior (cyan again). All mapping calculations use the various input fields shown in Fig. 1 which are however omitted here for clarity.

More technically, the mappings also need a linearization of the non-linear dependence of pCO_2 on DIC, consisting of three fields (the derivatives $dpCO_2/dDIC$ as well as reference fields for pCO_2 and DIC) together depicted by the grey arrows. Box L denotes the calculation of $dpCO_2/dDIC$ and the reference DIC field from a reference pCO_2 field (light blue) as described in Sect. 2.1.6 (the further input fields required by this calculation are not depicted). For the main mappings M_{ZE}, M_E, M_R, and M_H, the reference pCO_2 field comes from the data-based estimate of the pre-mapping M_P. The linearization for M_P, in turn, uses the atmospheric pCO_2 field as pCO_2 reference (light blue again).
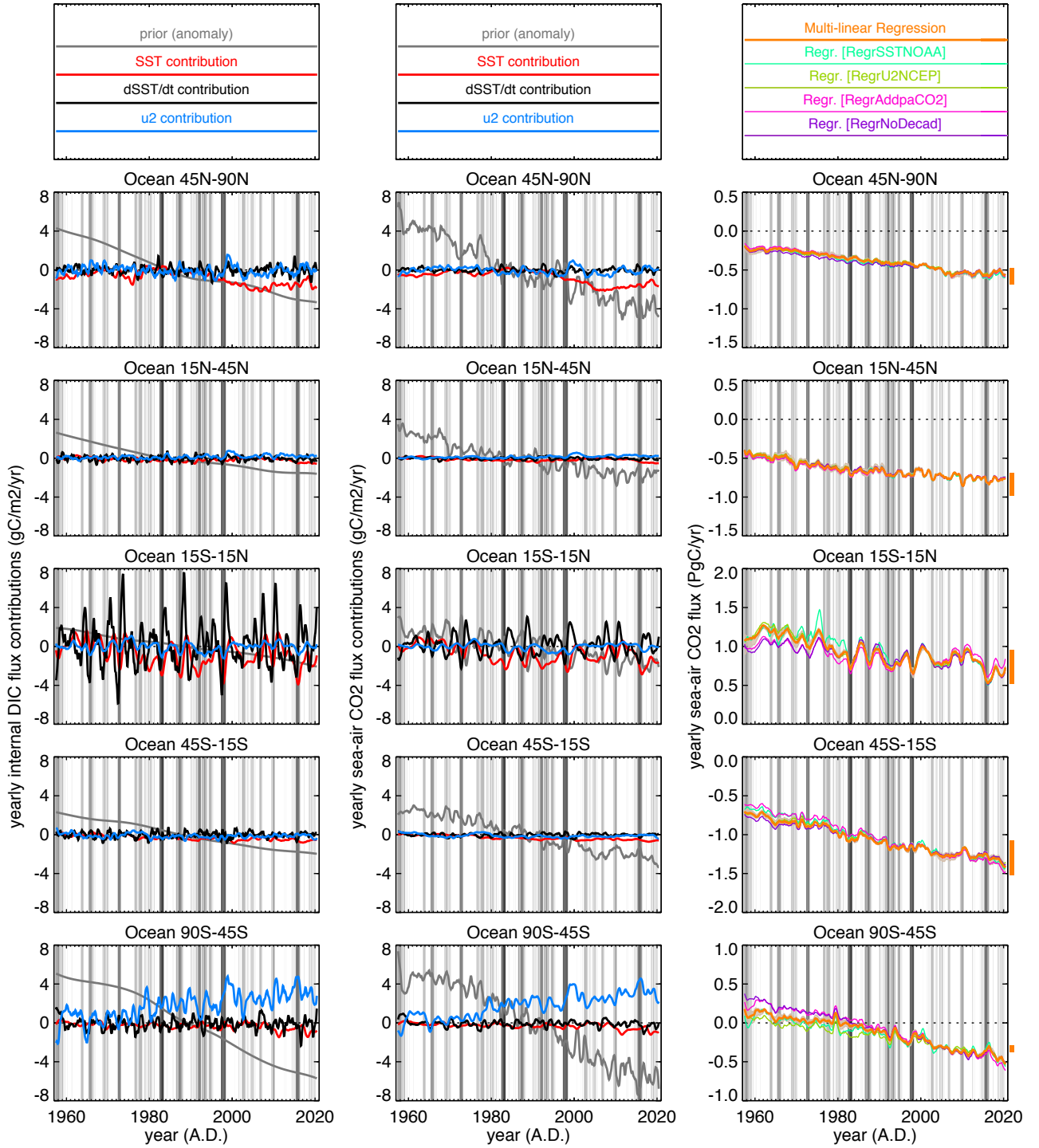
Figure 3. *Left:* Estimated contributions of the three explanatory variables in the multi-linear regression (as well as the prior, plotted here without its mean) to the ocean-internal DIC flux in 5 latitudinal bands (top to bottom). *Center:* Corresponding contributions to the sea–air CO_2 flux. *Right:* Total sea–air CO_2 flux estimated by the multi-linear regression (base case, orange) together with the uncertainty cases listed in Sect. 2.2 (the cases with the largest impact on interannual variability [RegrSSTNOAA, RegrU2NCEP, RegrAddpaCO2, RegrNoDecad] are plotted explicitly in different colors; since the cases related to gas exchange [GasexLow, GasexHigh, GasexU1, GasexU3] shift the long-term mean of the flux, the range of this shift has been indicated by the length of the vertical orange bars just to the right of each panel for clarity; the remaining uncertainty cases having rather small impact [RegrAdddSSTdt2, RegrAddU4, RegrLoose, RegrShort, MLDq2,
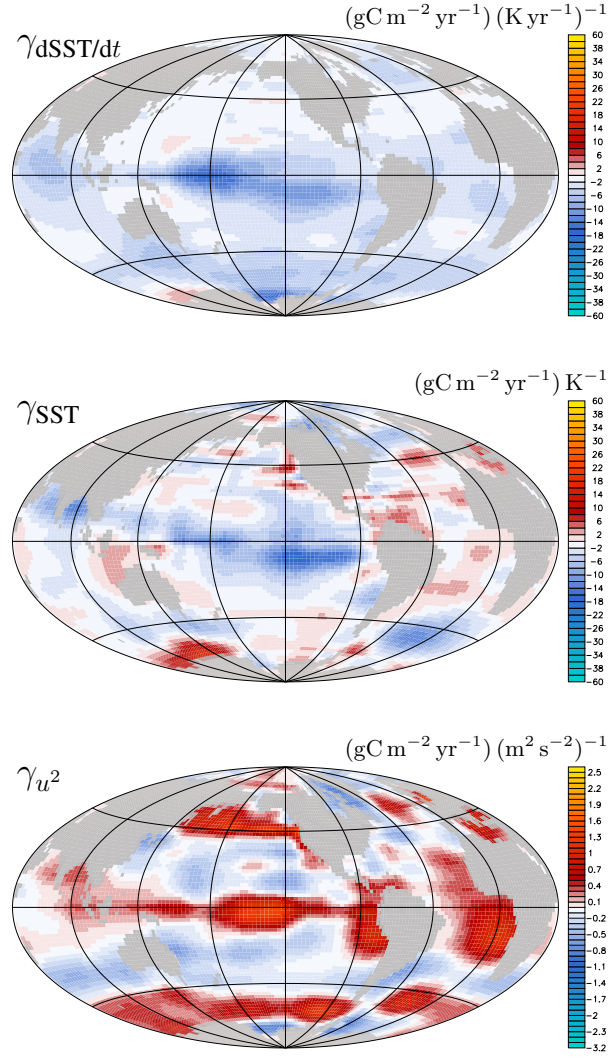
Figure 4. Estimated sensitivities of the ocean-internal DIC flux f_{int} against interannual variations in the temporal changes in sea surface temperature (top), in the sea surface temperature itself (middle), and in squared wind speed (bottom). Positive (negative) sensitivities mean that increases in the respective explanatory variable are associated with a stronger source (stronger sink) of DIC in the mixed layer.
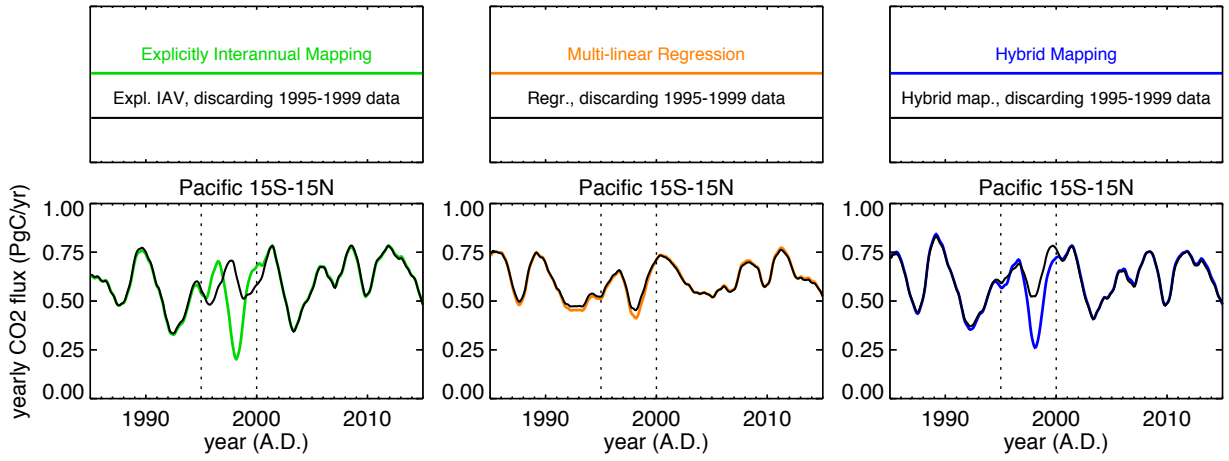
Figure 5. Interannual variations of the sea–air CO_2 flux in the tropical Pacific estimated by the explicitly interannual mapping (left), the multi-linear regression (center), and the hybrid mapping (right), either using all pCO_2 data (base cases, color) or all data but the ones during 1995–1999 (black)
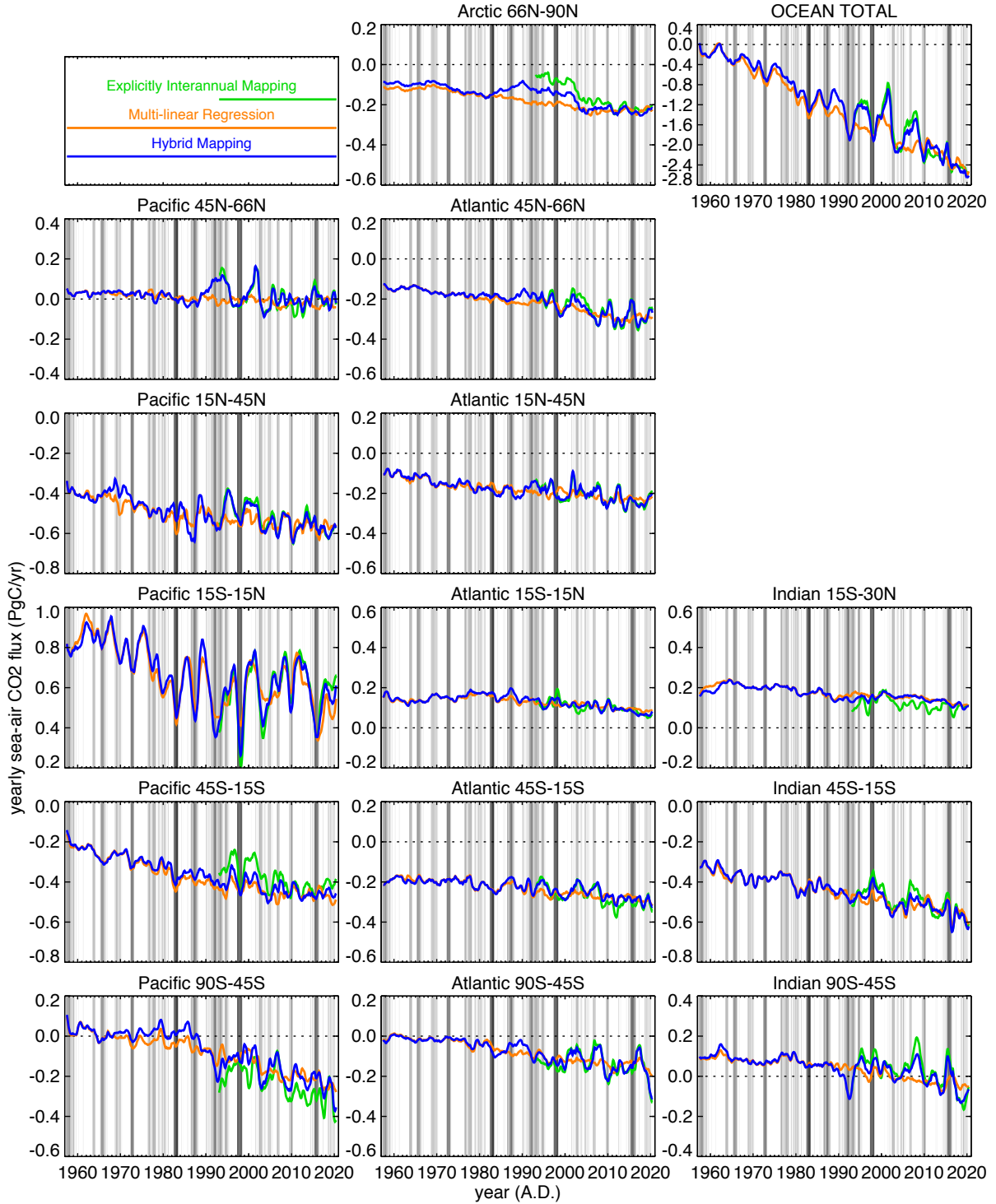
Figure 6. Yearly sea–air CO_2 flux as estimated from pCO_2 data by the explicitly interannual mapping (green, discarded before 1985 when the data constraint is very weak), the multi-linear regression (orange), and the hybrid mapping (blue). Fluxes have been integrated over a set of regions subdividing the ocean into basins (left to right) and latitude bands (top to bottom). For better temporal orientation across panels, the grey vertical background stripes indicate the positive phases of El Niño-Southern Oscillation according to the Multivariate El Niño Index (MEI) by Wolter and Timlin (1993).
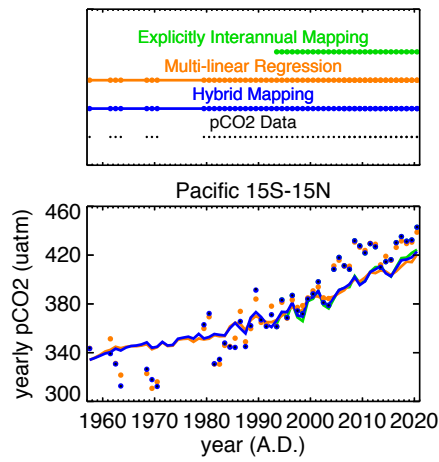
Figure 7. Estimated $p\mathrm{CO_2}$ in the tropical Pacific, averaged spatially and over calendar years. The coloured *lines* give full regional averages from the explicitly interannual mapping (green), the multi-linear regression (orange), and the hybrid mapping (blue). The coloured *dots* are from the same estimates, but averaged only over the pixels and time steps covered by $p\mathrm{CO_2}$ data in the respective year. The smaller black dots give the corresponding averages over the data. We note that the green, blue, and black dots are not visible individually because they are almost exactly located on top of each other, indicating that the model–data residuals of the explicitly interannual and hybrid mappings are very small. The differences between dots and lines reflect the bias of the incompletely sampled average compared to the full regional average, which the mapping algorithm is trying to address.
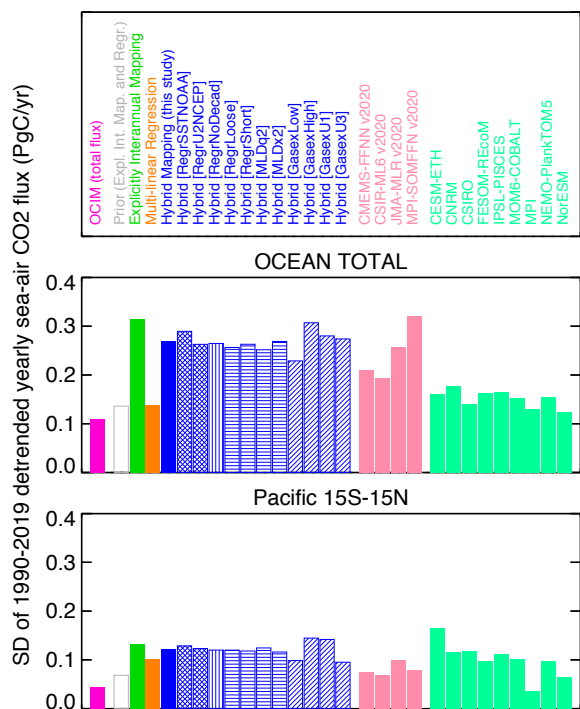
Figure 8. Amplitudes of variability of the sea–air CO_2 flux on year-to-year time scales around its secular trend, from the multi-linear regression (orange group of bars; solid: base case, hashed: uncertainty cases) and the hybrid mapping (blue) compared to other pCO_2 mapping methods (salmon; CMEMS v2020 (Denvil-Sommer et al., 2019), CSIR-ML6 v2020 (Gregor et al., 2019), JMA-MLR v2020 (Iida et al., 2020), and MPI-SOMFFN v2020 (Landschützer et al., 2013)) as well as the ocean biogeochemical process models collated in Friedlingstein et al. (2020) (mint green). The amplitudes are represented by temporal standard deviations of detrended yearly fluxes over the 1990–2019 period. The top panel gives the global flux, the bottom panel the tropical Pacific.
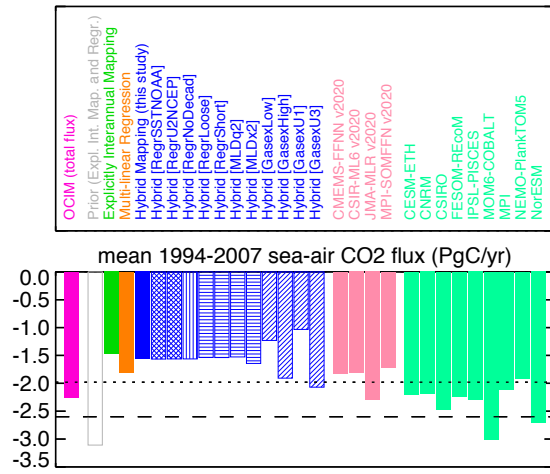
Figure 9. Mean global sea–air CO_2 flux over 1994–2007 from the hybrid mapping (blue group of bars; solid: base case, hashed: uncertainty cases), compared to other pCO_2 mapping methods (salmon; CMEMS v2020 (Denvil-Sommer et al., 2019), CSIR-ML6 v2020 (Gregor et al., 2019), JMA-MLR v2020 (Iida et al., 2020), and MPI-SOMFFN v2020 (Landschützer et al., 2013)), and the ocean biogeochemical process models collated in Friedlingstein et al. (2020) (not including a river-induced sea–air flux [see Table 3], mint green). To the left of the hybrid mapping, we also give OCIM (DeVries, 2022, total contemporary flux) as well as intermediate results from this study. The long-dashed horizontal line indicates the estimate of $-2.6 \pm 0.4\,\mathrm{PgC\,yr^{-1}}$ from ocean interior data by Gruber et al. (2019, anthropogenic carbon only), and the dotted line the same estimate shifted by $0.62\,\mathrm{PgC\,yr^{-1}}$ (mid of Jacobson et al. (2007) and Resplandy et al. (2018)) as an assumed contribution from outgassing of terrestrial carbon transported to the ocean by rivers. Positive fluxes denote oceanic CO_2 outgassing into the atmosphere, negative fluxes denote CO_2 sinks into the ocean.
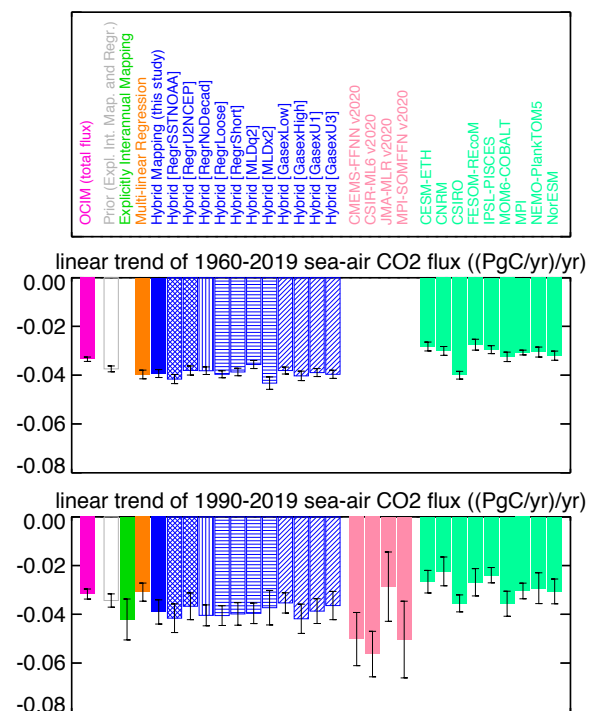
Figure 10. Secular linear trend of the global sea–air CO_2 flux over 1960–2019 (*top*) and over the more recent 1990–2019 period better constrained by pCO_2 data (*bottom*), from the same estimates as in Fig. 9. The error bars give the formal error of the slope calculated from 5-year flux averages, i.e., they reflect the uncertainty due to the pentadal variability around the linear trend, thereby roughly taking into account the serial correlations of the flux e.g. on the El Niño time scale
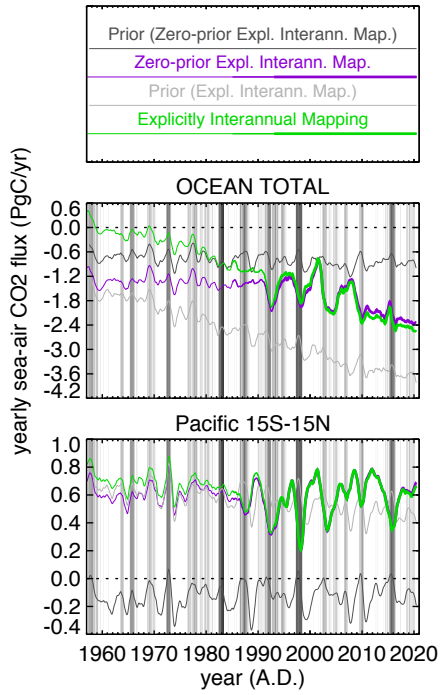
Figure 11. Interannually filtered sea–air fluxes as in Fig. 6 (2 example panels only) estimated by the zero-prior explicitly interannual pCO_2 mapping (violet) and the explicitly interannual pCO_2 mapping (green), as well as their respective priors (dark and light grey, respectively; note that the designation "zero-prior" refers to $f_{int}^{ZE,pri} = 0$, while the a-priori sea–air fluxes shown here are in fact non-zero owing to the rise in atmospheric CO_2 and the variations in SST). The line width roughly distinguishes the early period with insufficient data constraint (thin) and the more recent period with better constraint (thick). Vertical background stripes as in Fig. 6